

The ALPINE-ALMA [C II] survey: Characterisation of Spatial Offsets in Main-Sequence Galaxies at $z \sim 4\text{--}6$

Meghana Killi,^{1,2,3,4*} Michele Ginolfi,^{5,6} Gergő Popping,³ Darach Watson,^{1,2} Giovanni Zamorani,⁷ Brian C. Lemaux,^{8,9} Seiji Fujimoto,¹⁰ Andreas Faisst,¹¹ Matthieu Bethermin,^{12,13} Michael Romano,^{14,15} Yoshinobu Fudamoto,^{16,17} Sandro Bardelli,⁷ Médéric Boquien,¹⁸ Stefano Carniani,¹⁹ Miroslava Dessauges-Zavadsky,²⁰ Carlotta Gruppioni,²¹ Nimish Hathi,²² Eduardo Ibar,²³ Gareth C. Jones,²⁴ Anton M. Koekemoer,²² Ivanna Langan,^{3,25} Hugo Méndez-Hernández,^{26,27} Yuma Sugahara^{16,17} Livia Vallini,⁷ Daniela Vergani²¹

¹Cosmic Dawn Center (DAWN), Jagtvej 128, 2200 Copenhagen N, Denmark

²Niels Bohr Institute, University of Copenhagen, Lyngbyvej 2, 2100 Copenhagen Ø, Denmark

³European Southern Observatory, Karl-Schwarzschild-Straße 2, 85748 Garching bei München, Germany

⁴Instituto de Estudios Astrofísicos, Facultad de Ingeniería y Ciencias, Universidad Diego Portales, Av. Ejército 441, Santiago 8370191, Chile

⁵Dipartimento di Fisica e Astronomia, Università di Firenze, Via G. Sansone 1, 50019, Sesto Fiorentino (Firenze), Italy

⁶INAF - Osservatorio Astrofisico di Arcetri, Largo E. Fermi 5, I-50125, Firenze, Italy

⁷INAF – Osservatorio di Astrofisica e Scienza dello Spazio, Via P. Gobetti 93/3, I-40129 Bologna, Italy

⁸Department of Physics and Astronomy, University of California, Davis, One Shields Ave., Davis, CA 95616, USA

⁹Gemini Observatory, NSF’s NOIRLab, 670 N. A’ohoku Place, Hilo, Hawai’i 96720, USA

¹⁰Department of Astronomy, The University of Texas at Austin, 2515 Speedway Blvd Stop C1400, Austin, TX 78712, USA

¹¹IPAC, California Institute of Technology, 1200 East California Boulevard, Pasadena, CA 91125, USA

¹²Aix Marseille Univ, CNRS, CNES, LAM, Marseille, France

¹³Université de Strasbourg, CNRS, Observatoire astronomique de Strasbourg, UMR 7550, 67000, Strasbourg, France

¹⁴National Centre for Nuclear Research, ul. Pasteura 7, 02-093 Warsaw, Poland

¹⁵INAF - Osservatorio Astronomico di Padova, Vicolo dell’Osservatorio 5, I-35122, Padova, Italy

¹⁶National Astronomical Observatory of Japan, 2-21-1 Osawa, Mitaka, Tokyo 181-8588, Japan

¹⁷Waseda Research Institute for Science and Engineering, Faculty of Science and Engineering, Waseda University, 3-4-1, Okubo, Shinjuku, Tokyo 169-8555, Japan

¹⁸Centro de Astronomía (CITEVA), Universidad de Antofagasta, Avenida Angamos 601, Antofagasta, Chile

¹⁹Scuola Normale Superiore, Piazza dei Cavalieri 7, I-56126 Pisa, Italy

²⁰Department of Astronomy, University of Geneva, Chemin Pegasi 51, 1290 Versoix, Switzerland

²¹Istituto Nazionale di Astrofisica: Osservatorio di Astrofisica e Scienza dello Spazio di Bologna, Via Gobetti 93/3, 40129 Bologna, Italy

²²Space Telescope Science Institute, Baltimore, MD 21218, USA

²³Instituto de Física y Astronomía, Universidad de Valparaíso, Avda. Gran Bretaña 1111, Valparaíso, Chile

²⁴Department of Physics, University of Oxford, Denys Wilkinson Building, Keble Road, Oxford OX1 3RH, UK

²⁵Univ Lyon, Univ Lyon1, Ens de Lyon, CNRS, Centre de Recherche Astrophysique de Lyon (CRAL) UMR5574, F-69230 Saint-Genis-Laval, France

²⁶Instituto Multidisciplinario de Investigación y Postgrado, Universidad de La Serena, Raúl Bitrán 1305, La Serena, Chile

²⁷Departamento de Astronomía, Universidad de La Serena, Av. Juan Cisternas 1200 N, La Serena, Chile

Accepted XXX. Received YYY; in original form ZZZ

ABSTRACT

Galaxy morphology is shaped by stellar activity, feedback, gas and dust properties, and interactions with surroundings, and can therefore provide insight into these processes. In this paper, we study the spatial offsets between stellar and interstellar medium emission in a sample of 54 main-sequence star-forming galaxies at $z \sim 4\text{--}6$ observed with the Atacama Large Millimeter/submillimeter Array (ALMA) and drawn from the ALMA Large Program to INvestigate C⁺ at Early times (ALPINE). We find no significant spatial offset for the majority (~ 70 percent) of galaxies in the sample among any combination of [C II], far-infrared continuum, optical, and ultraviolet emission. However, a fraction of the sample (~ 30 percent) shows offsets larger than the median by more than 3σ significance (compared to the uncertainty on the offsets), especially between [C II] and ultraviolet emission. We find that these significant offsets are of the order of $\sim 0.5\text{--}0.7$ arcsec, corresponding to $\sim 3.5\text{--}4.5$ kiloparsecs. The offsets could be caused by a complex dust geometry, strong feedback from stars and active galactic nuclei, large-scale gas inflow and outflow, or a combination of these phenomena. However, our current analysis does not definitively constrain the origin. Future, higher resolution ALMA and JWST observations may help resolve the ambiguity. Regardless, since there exist at least some galaxies that display such large offsets, galaxy models and spectral energy distribution fitting codes cannot assume co-spatial emission in all main-sequence galaxies, and must take into account that the observed emission across wavelengths may be spatially segregated.

Key words: galaxies: evolution – galaxies: high-redshift – galaxies: ISM – galaxies: statistics

1 INTRODUCTION

The redshift 6 to 4 era corresponds to the period between the end of reionisation of the Universe where the earliest galaxies lived (e.g. Fan et al. 2006; Dayal et al. 2018; Robertson 2022), and the beginning of cosmic noon where the bulk of the Universe’s stellar mass was created (e.g. Förster Schreiber & Wuyts 2020). This transition period is therefore of utmost interest to trace the evolution of galaxies from first light to the present day.

The most representative galaxies at $z \sim 4\text{--}6$ are those that populate the star-forming main sequence relation (between stellar mass, M_\star , and star-formation rate, SFR) at these redshifts (e.g. Noeske et al. 2007; Speagle et al. 2014; Popesso et al. 2022), and should hence be ideal to study the physics that led to the eventual creation of modern galaxies. Since observations based only on ultraviolet (UV) emission are limited by dust attenuation (Fudamoto et al. 2020, 2021), comprehensive studies of main-sequence galaxies and their dust properties require far-infrared (FIR) continuum observations with e.g. the Atacama Large Millimeter/sub-millimeter Array (ALMA). ALMA also allows the study of the cold gas component through observations of bright rest-frame FIR emission lines such as [C II] 158 μm , a major coolant of the interstellar medium (ISM; Hollenbach & Tielens 1999; Wolfire et al. 2022), generally emitted from multiple gas phases (ionised, neutral, and molecular gas; Carilli & Walter 2013; Vallini et al. 2013, 2017; Lagache et al. 2018; Zanella et al. 2018).

Understanding the physics occurring within galaxies requires the study of both stellar and ISM phases at high-resolution, but it is observationally expensive to conduct high-resolution studies at these redshifts. An alternative is to study the spatial offset between centroids of emission at different wavelengths, which can be done even with low-resolution observations. The presence or absence of spatial offset in a given galaxy can reveal how the stellar and ISM phases evolve and interact. Characterising offsets in a statistical sample of main-sequence galaxies can tell us what is normal among high- z galaxies, and separate the exceptional from the ordinary. We may then study the physics that produces these exceptions, and trace its influence on galaxy evolution.

A few recent studies have found spatial offsets of the order of a few kiloparsecs (kpc) among stellar emission (from H II regions/ionised diffuse gas traced by rest-frame UV/optical continuum or [O III]), ISM gas emission (from metal-enriched/molecular gas traced by [C II] or CO), and ISM dust emission (traced by the FIR continuum) in galaxies at $z \sim 4\text{--}6$ (Hodge et al. 2012; Willott et al. 2015; Pentericci et al. 2016; Carniani et al. 2018; Matthee et al. 2019; Fujimoto et al. 2020) and beyond, up to $z \sim 8.5$ (Maiolino et al. 2015; Laporte et al. 2017; Carniani et al. 2017; Fujimoto et al. 2022a; Schouws et al. 2022; Bowler et al. 2022; Inami et al. 2022). Several state-of-art zoom-in cosmological simulations have also consistently found spatial displacement of a similar scale between [C II]/IR bright regions and [O III]/UV bright regions in the ISM of $z\sim 5\text{--}6$ galaxies (e.g. Arata et al. 2019; Katz et al. 2017; Behrens et al. 2018; Katz et al. 2019; Pallottini et al. 2019; Sommovigo et al. 2020; Pallottini et al. 2022). While some predict that offsets should be commonplace as the processes driving them are ubiquitous, others suggest that the offset phenomenon is transient, and therefore observation of offsets should be rare.

In this context, a statistical observational study to identify what fraction of high- z , main-sequence galaxies display stellar-ISM spatial offsets is yet to be conducted. This knowledge is important because spectral energy distribution (SED) fitting models often assume an energy balance between emission in the UV and FIR (or at least that the emission in UV/optical is coupled to that in FIR) to derive galaxy

properties such as stellar mass (M_\star), star-formation rate (SFR), and dust content (e.g. Da Cunha et al. 2008; Boquien et al. 2019). This assumption may not hold when there is a spatial offset causing a segregation of UV and FIR emission.

In order to conduct a systematic study of spatial offsets, we use the ALPINE-ALMA [C II] survey (ALMA Large Programme to INvestigate C+ at Early times; Béthermin et al. 2020; Le Fèvre et al. 2020; Faisst et al. 2020), which is a statistically significant (see Sec. 2.1) sample of main-sequence galaxies at $z \sim 4\text{--}6$. In addition to the FIR properties from ALMA, ALPINE is also covered by a wealth of ancillary data from rest-frame UV to mid-IR, making it an ideal sample to perform this analysis.

We calculate spatial offsets between pairs of emissions, and provide a statistical characterisation of the number, significance, and size of the offsets. We then identify galaxies with significant spatial offsets between stellar and ISM emission, and investigate any potential correlations between offsets and galaxy physical properties, e.g. M_\star , SFR, and dust attenuation.

We adopt a Flat Λ CDM cosmology with $H_0 = 70 \text{ km s}^{-1} \text{ Mpc}^{-1}$, $\Omega_M = 0.3$, and $\Omega_\Lambda = 0.7$. For this cosmology, $1'' = 6.27 \text{ kpc}$ at $z = 5$, i.e., the mean redshift of our study.

2 SAMPLE AND DATA REDUCTION

2.1 Basic properties of the full ALPINE sample

The full ALPINE (Project ID: 2017.1.00428.L; PI: O. Le Fèvre) sample consists of 118 main-sequence star-forming galaxies at $4.4 < z < 5.9$, excluding the low-transmission (for [C II]) atmospheric window between $4.6 < z < 5.1$. The targets were selected using spectroscopic redshifts based on Lyman- α and UV ISM lines (Faisst et al. 2020), and were drawn from the Cosmic Evolution Survey (COSMOS; Scoville et al. 2006a,b), the Extended Chandra Deep Field South (ECDFS; Cardamone et al. 2010), and the Great Observatories Origins Deep Survey (GOODS; Giavalisco & Team 2003) fields.

The [C II] and FIR continuum data consist of ~ 70 hours of ALMA Band 7 observations conducted in cycles 5 and 6. These emissions trace the metal-enriched cold gas and the dust respectively (e.g. Grupioni et al. 2020; Ginolfi et al. 2020; Pozzi et al. 2021). The ALMA data-cubes were reduced and calibrated using the standard Common Astronomy Software Applications (CASA; McMullin et al. 2007) pipeline. Each cube was continuum-subtracted in the uv -plane, and a line search algorithm was then applied to detect the [C II] line with $\text{SNR} > 3.5$. ALPINE cubes and images have a pixel scale of $0.15 \text{ arcsec pixel}^{-1}$ and a 1σ sensitivity on the integrated [C II] luminosity $L_{[\text{CII}]}$ of $0.4 \times 10^8 L_\odot$ assuming a line width of 235 km s^{-1} . The smallest circularised beams of galaxies in the dataset are of the order of 0.8 arcsec , while the largest are of the order of 1.5 arcsec .

For further details on the data reduction, see Béthermin et al. (2020). The ALMA data products (moment maps and continuum images) are publicly available through the ALPINE Data Release 1 repository¹.

In addition to [C II] and FIR continuum images, we use rest-frame UV images from the Hubble Space Telescope (HST) taken with the Advanced Camera for Surveys (ACS) F814W filter (Scoville et al. 2006a; Koekemoer et al. 2007, 2011) to trace the young, massive stellar population. These observations have a 3σ depth of $\sim 29 \text{ mag}$

¹ https://cesam.lam.fr/a2c2s/data_release.php

Emission tracer	Number	Fields
UV	54	COSMOS, GOODS-S, ECFDS
Optical	45	COSMOS
[C II]	52	COSMOS, GOODS-S, ECFDS
FIR continuum	16	COSMOS, GOODS-S, ECFDS

Table 1. Number of galaxies in our sample with each emission tracer observation, and the fields in which the galaxies are located

[AB], with a pixel scale of $0.06 \text{ arcsec pixel}^{-1}$, and all *HST* images are registered to Gaia DR2 (Faisst et al. 2020).

We also include K-band emission from the UltraVISTA survey (McCracken et al. 2012) Data Release 4 (Moneti et al. 2023) to trace a slightly older stellar population (compared to that seen with *HST*/F814W). The K-band ($\sim 2.2 \mu\text{m}$) emission may come from either the rest-frame optical or the near-UV part of a galaxy’s spectrum, depending upon its redshift (between 330 nm and 400 nm for ALPINE), but we refer to it as the “optical” emission throughout this paper. The spatial resolution for these images is in the range 0.74–0.78 arcsec, with a seeing of ~ 0.64 arcsec, and a limiting magnitude of 24.9 [AB] (computed as the 5σ limit in a 2.0 arcsec aperture, Moneti et al. 2019). The images have a pixel scale of $0.15 \text{ arcsec pixel}^{-1}$ (McCracken et al. 2012), the same as the ALPINE [C II] and FIR continuum images.

Galaxy physical properties were presented by Faisst et al. (2020). UV continuum and absorption line properties were obtained from imaging and spectroscopy with *HST*, Keck, and various other instruments, optical lines were inferred from Spitzer photometry, and FIR lines from ALMA. M_\star , SFR, light-weighted stellar population age, absolute magnitude, optical dust reddening, and UV continuum slope were obtained via SED fitting with the LePhare code (Arnouts et al. 1999; Ilbert et al. 2006; Arnouts & Ilbert 2011), using synthetic templates based on the Bruzual & Charlot (2003) stellar population library, tuned to represent galaxies at $4 < z < 6$. ALPINE galaxies were found to span a range of stellar masses ($\log(M_\star/M_\odot) \sim 9\text{--}11$) and SFRs ($\log(\text{SFR}/M_\odot\text{yr}^{-1}) \sim 1\text{--}3$). $H\alpha$ emission properties including line luminosity and equivalent width were obtained from the Spitzer $[3.6 \mu\text{m}]$ – $[4.5 \mu\text{m}]$ colour. $H\alpha$ luminosity was in turn used to derive an estimate of the SFR using the Kennicutt (1998) relation. [C II]–ISM velocity offsets were determined by Cassata et al. (2020). For further information on the reduction and properties of ALPINE ancillary data, see Faisst et al. (2020).

2.2 Our sample

Of the 118 ALPINE galaxies, 75 were detected in [C II] emission, and 23 in FIR continuum (21 galaxies have both [C II] and FIR continuum detection). Romano et al. (2021) performed a morphokinematic classification based on [C II] emission to identify mergers and multi-component systems and found 23 such merging sources. It is important to note that while their analysis excludes *major* mergers that can be discerned at our current resolution, there may still be minor or close mergers, satellites, accretion, and clumps at smaller scales. Moreover, as these mergers were identified based mostly on [C II] emission, there may still be multiple components in the continuum, optical, or UV emission (see Sec. 5.1.2). For the purpose of this paper, we will exclude the mergers identified as such in Romano et al. (2021) (cross-checked with the “MER” class in Jones et al. (2021)), which is a subset of mergers from Romano et al. (2021)) and only consider the remaining population.

This “non-merging” ALPINE sample consists of 54 galaxies, of which 52 have [C II] detection, and 16 have FIR continuum detection

(14 galaxies have both [C II] and FIR continuum detection; CANDELS_GOODSS_19 and DEIMOS_COSMOS_460378 have FIR continuum but no [C II] detection). All 54 galaxies have UV observations with *HST*. 45 of these sources, covered by the COSMOS field, have deep UltraVISTA observations in the K-band (the remaining 9 sources in ECFDS and GOODS-S are excluded as they are not detected or barely detected in K-band). 12 galaxies in COSMOS have detections in all four emissions. In Table 1, we show the distribution of the final sample, indicating the number of galaxies that have observations in the UV, optical, [C II], and FIR continuum.

3 METHODS

In this section, we describe the methods used in this work to calculate centroids of emission in the four emission tracers, and derive spatial offsets among them.

3.1 UV centroids

We use *HST* images taken with the ACS/F814W filter (see Sec. 2.1), tracing rest-frame UV emission at the redshift of our targets. The UV centroids are assumed to be the *HST* RA and Dec coordinates from the Faisst et al. (2020) catalogue. For each galaxy, an astrometric correction is provided in this catalogue as δRA and δDec values to be added to the *HST* coordinates so that the image is aligned with the Gaia DR2 (Mignard et al. 2018) catalogue. Faisst et al. (2020) find an additional scatter of ~ 30 mas in both RA and Dec after the astrometric correction is applied. We calculate the total UV centroid uncertainty as the sum in quadrature of uncertainty on RA and Dec, which amounts to ~ 40 mas for all UV images.

3.2 Centroid fitting and uncertainty

For [C II], FIR continuum, and optical images, we find the centroid of emission and estimate uncertainties in the following way.

3.2.1 [C II] and FIR continuum

For each galaxy detected in [C II] or FIR continuum (or both), we crop the corresponding ALMA moment-0 and/or continuum maps into cutouts of 6.0×6.0 arcsec (40×40 pixels) around the UV centroid position (see Sec. 3.1). To estimate the typical noise level in the image, we calculate the sigma clipped standard deviation of pixel values within an annulus of inner and outer radii of 4.5 and 9.0 arcsec (30 and 60 pixels). We use this to apply a 2σ masking to the cutout image and exclude pixels that are below this significance level. For the pixels with significance $> 2\sigma$, we fit a two-dimensional, elliptical Gaussian of the form

$$f(x, y) = Ae^{-(a(x-x_0)^2 + 2b(x-x_0)(y-y_0) + c(y-y_0)^2)}, \quad (1)$$

where

$$a = \frac{\cos^2(\theta)}{2\sigma_x^2} + \frac{\sin^2(\theta)}{2\sigma_y^2}, \quad (2)$$

$$b = -\frac{\sin(2\theta)}{4\sigma_x^2} + \frac{\sin(2\theta)}{4\sigma_y^2}, \quad (3)$$

and

$$c = \frac{\sin^2(\theta)}{2\sigma_x^2} + \frac{\cos^2(\theta)}{2\sigma_y^2}. \quad (4)$$

Here, x_0, y_0 are the coordinates of the centre, σ_x, σ_y are the Gaussian widths along each dimension, and θ is the counter-clockwise angle.

We use `SCIPY.OPTIMIZE.CURVE_FIT` (Virtanen et al. 2020) to perform the fitting. The initial guesses for the parameters A, x_0 , and y_0 are obtained by finding the brightest pixel within a 1.5 arcsec (10 pixel) cutout around the coordinates of the UV centroids (Sec. 3.1). The initial guesses for σ_x, σ_y and θ are the same for all images, at 2 px, 2 px, and 0° respectively. We then let `CURVE_FIT` fit a 2D Gaussian to the masked image starting with the above initial parameters. If the fit converges, the fit centroid is defined as the centre of the 2D Gaussian, (x_0, y_0) .

We find fit uncertainties using a bootstrapping method with 100 trials per galaxy. We first add random Gaussian (with mean ~ 0 and $\sigma \sim$ noise level in the image) noise to each pixel in the input image for each trial, and create 100 “noisy images” per galaxy. For each noisy image, we repeat the 2D Gaussian fitting procedure described above, including the noise estimation, 2σ masking, initial guess, and Gaussian fit. We exclude trials where the fit fails to converge (which happens for <3 trials out of 100 in our analysis). Then the average centre position over all converged trials gives the final centroid position of the galaxy. The standard deviation among converged trials gives the 1σ fit uncertainty on the x and y positions of the centroid. The fit error is then obtained as the sum in quadrature of the x and y uncertainty.

For the continuum emission of DEIMOS_COSMOS_881725 and VUDS_ECDFS_530029038, we perform the fitting in a smaller crop extent of 2.25 arcsec (15 pixels) on a side to avoid nearby bright sources.

To test the robustness of our centroid estimate, we also fit a 2D Sersic to the images, using a Sersic model instead of a Gaussian in our fitting code above. The centroids thus obtained agree with our 2D Gaussian centroids to within one pixel, i.e., less than a kpc. We also vary the masking criterion from 1σ to 3σ . The centroids again agree to within ~ 1.5 kpc. We choose the 2σ masking for our final fits to avoid being unduly influenced by spurious noise features, while at the same time not biasing the result towards the peak pixel.

As a sanity check, we compare the brightest source pixel in each image (i.e., the “peak” pixel supplied as the initial guess on the x and y coordinates to the centroid fitting code) and the centre of light (`SCIPY.NDIMAGE.CENTER_OF_MASS`, Virtanen et al. 2020) with the centroid obtained from the fit. We find that the peak pixel and centre of light generally trace the fit centroid position. The peak is found to be within 2 kpc of the 2D Gaussian (and 2D Sersic) centroids. The centre of light is more susceptible to influence by nearby sources and noise fluctuations, with a large scatter (less than 1 kpc for high SNR images, and up to ~ 5.5 kpc for images with bright nearby sources and strong noise features), but generally following the 2D Gaussian centroid positions.

3.2.2 Optical

For optical images, we use the same procedure as for the [C II] and FIR continuum to find centroids and uncertainties, with the exception of the crop extent. We use various crop extents between 2.25 and 4.50 arcsec (15 and 30 pixels) to perform the optical centroid fits, so as to avoid other bright sources close to the target galaxy. Despite these measures, several galaxies (vuds_cosmos_510596653, vuds_cosmos_5101288969, DEIMOS_COSMOS_357722, DEIMOS_COSMOS_722679, and DEIMOS_COSMOS_843045) fail to fit or return a poor fit (either due to high noise in the image or the presence of bright sources very

close to the target galaxy). We therefore exclude the optical emission of these galaxies from further analysis.

In Fig. 1, we show an example of centroid fits to emission in [C II], FIR continuum, and optical emission for the galaxy VUDS_COSMOS_5101218326.

3.2.3 Positional accuracy

In addition to the fit error, there is positional uncertainty associated with telescope pointings, which contributes to the uncertainty on the centroid position. The positional uncertainty for optical centroids is taken as 80 mas in both RA and Dec (McCracken et al. 2012), resulting in a total positional uncertainty of ~ 110 mas.

For ALMA images, the positional accuracy Δp (in milliarcsec) is given by Eq. 3 of Faisst et al. (2020):

$$\Delta p = \frac{70000}{\nu B \sigma_{peak}} \quad (5)$$

where ν is the observed frequency in GHz, B is the maximum baseline length in kilometers, and σ_{peak} is the calibrator SNR at the peak of the emission. For the ALPINE data, $B = 0.2$ km corresponding to the C43-1 configuration, ν is ~ 330 GHz, and σ_{peak} is ~ 50 , which results in a Δp of ~ 20 mas. We use this value as the positional uncertainty on the [C II] and FIR continuum centroids.

3.2.4 Noise correlation at the beam scale

For ALMA images, noise is correlated on the scale of the beam (which is the same size as most of our marginally resolved objects), which introduces additional uncertainty in determining the centroid position. We estimate this uncertainty in the following way. We first inject several artificial 2D elliptical Gaussian galaxies of the same form as in Eq. 1 into each [C II] and FIR continuum image around the central source. The 2D Gaussian height, widths in x and y , and position angle of the injected sources are chosen to be random values within 1σ of the corresponding properties of the real source in the image as recovered by our fitting in Sec. 3.2.1. The centre positions (x_0, y_0) of the simulated galaxies are chosen at random within an annulus of 6 to 12 arcsec (40 to 80 pixels), around the centre of the image. We ensure that no two simulated galaxies are within five standard deviations of each other so that the flux from one does not influence the fit of another.

Then, we fit each of these simulated galaxies in the same way as we fit the real galaxy (as described in Sec. 3.2.1) within a crop extent of 3.0 arcsec (20 pixels). We introduce 20 simulated sources and average over 50 trials per source (a total of 1000 fits per image). We calculate the difference between injected and fit centroid position for each simulated galaxy, and then the sigma clipped median of these differences for all the simulated galaxies in each image. This value is taken as the noise correlation uncertainty (Δ_{NC}) for [C II] and FIR continuum centroids. Thus, Δ_{NC} is calculated individually for each ALPINE source, ensuring that the simulated sources reflect the Gaussian properties of the real source.

In Fig. 2, we plot Δ_{NC} calculated in each [C II] and FIR continuum image against the median peak SNR (i.e., height) of the injected Gaussians in that image. The plot follows an inverse relation (of the form $a + \frac{b}{x}$, where x is the peak SNR, and a and b are constants), where the images with the lowest SNR show the largest deviation between injected and fit centroid positions. This is expected because given that the sizes of noise peaks and troughs are comparable to the ALMA beam, the morphology of a low SNR source will be more easily perturbed by the noise, resulting in a larger positional offset

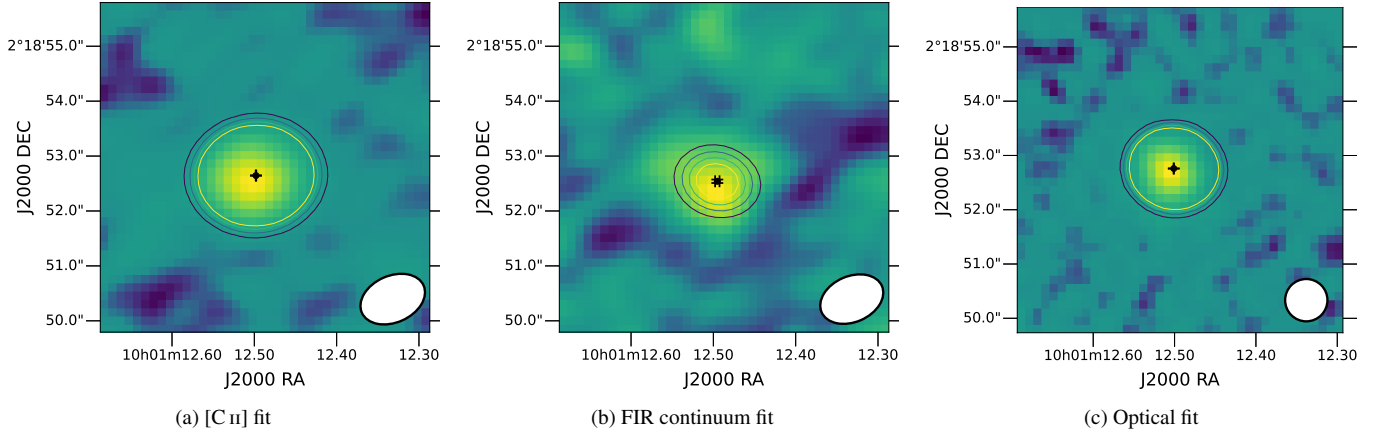


Figure 1. 2D Gaussian fits (shown as contours drawn at 2, 3, 4, and 5 σ) to find the centroids of (a) [C II], (b) FIR continuum, and (c) optical emission for the galaxy VUDS_COSMOS_5101218326. The fit uncertainty (without positional and Δ_{NC} uncertainties; see Sec. 3.2) on the x and y position of the centroid is also indicated with black errorbars. ALMA and optical beamsizes are shown as filled white ellipses.

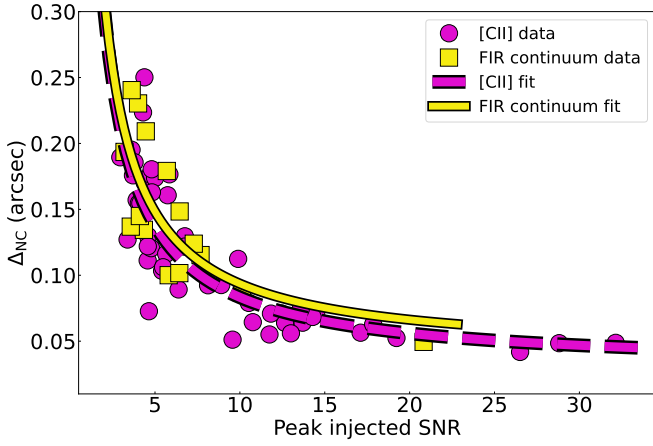


Figure 2. The inverse relationship between the noise correlation uncertainty (Δ_{NC} ; see Sec. 3.2.4) and median peak SNR of the injected Gaussians. The results for [C II] and FIR continuum images are shown in pink and yellow.

in the fit. Hence, the probability of positional offset of a fit has an anti-correlation with SNR.

3.2.5 Total uncertainty

The total uncertainty on the optical centroids is calculated as the sum in quadrature of the bootstrapped fit uncertainty (Sec. 3.2) and the positional uncertainty (Sec. 3.2.3). For the ALMA [C II] and FIR continuum centroids, the noise correlation term (Sec. 3.2.4) is also added in quadrature. In general, the noise correlation uncertainty dominates over the positional and fit uncertainties, especially for low SNR sources.

3.3 Spatial offsets

The spatial offset between any two emissions is defined as the spatial separation (in arcsec) between the calculated centroid positions of the two emissions. We use the `ASTROPY` (The Astropy Collaboration et al. 2022) function `COORDINATES.SKYCOORD.SEPARATION` to estimate this separation. The corresponding uncertainty on the offset is calculated as the sum in quadrature of the total positional uncertainties (see Sec. 3.2.5) on the centroids of the two emissions.

4 RESULTS

Given a Gaussian uncertainty σ on each coordinate (RA and DEC), the expected distribution of offsets (r) is given by a 2D circular Gaussian of the form:

$$f(r) dr = 2\pi r \left(\frac{1}{2\pi\sigma^2} \right) e^{-\frac{1}{2}\left(\frac{r}{\sigma}\right)^2} dr \quad (6)$$

$$= \left(\frac{r}{\sigma} \right) e^{-\frac{1}{2}\left(\frac{r}{\sigma}\right)^2} d\left(\frac{r}{\sigma} \right) \quad (7)$$

Calculating the significance (s) as measured offset divided by the measured total uncertainty, i.e., $s = \frac{r}{\sigma}$, we have,

$$f(r) dr = s e^{-\frac{1}{2}s^2} ds. \quad (8)$$

As the uncertainties for the various galaxies are not the same, we create a distribution in which each offset is normalised to its σ . We thus obtain an expected distribution of normalised offsets to compare with our observations (see Fig. 3). We adopt a 3σ threshold to identify offsets that are very likely to be real. In the following analysis, we will call these “significant” offsets. Based on the above expected distribution, the fraction of galaxies with no real offset having an observed significance of $s > 3$ should be 0.01. This corresponds to 0.01×54 (which is the total number of galaxies in our sample; see Sec. 2.2) ~ 0.5 , i.e., less than 1 galaxy. Therefore, we can be confident that all the galaxies in our sample with $s > 3$ have significant offsets unlikely to occur by chance. It is important to note that a significant offset is not necessarily a *large* offset, but it is significant compared to the uncertainty. In other words, the sensitivity and accuracy of our analysis increases with SNR.

4.1 Offset distributions

In Fig. 3, we show histograms of the significance of spatial offsets between combinations of [C II], UV, Optical, and FIR continuum. We plot the expected distribution as a normalised circular Gaussian (Eq. 8) and indicate our 3σ threshold using a grey shaded region. We find that for the majority of galaxies, the observed offsets could be caused by measurement uncertainties. However, some galaxies lie outside the expected distribution with a significance of $s > 3$.

Fig. 4 shows an example of one galaxy

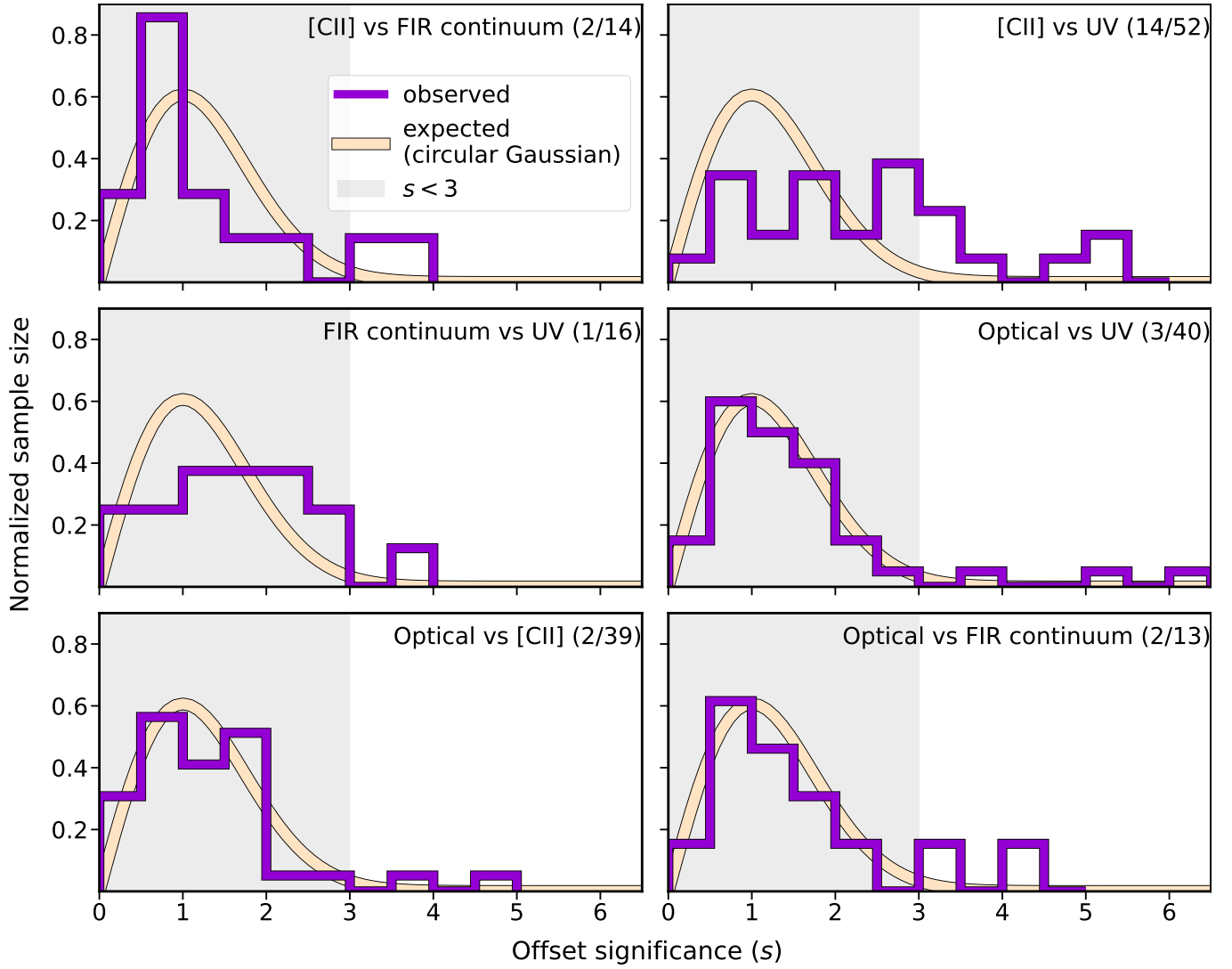


Figure 3. Normalised histograms of the significance (s) of observed spatial offsets between (from left to right; top) [C II]-FIR continuum, [C II]-UV, (middle) FIR continuum-UV, Optical-UV, (bottom) Optical-[C II], and Optical-FIR continuum emission are shown in violet. The cream-coloured curve is the expected distribution of offsets, modelled with a circular Gaussian (as described in Sec. 4). Although the majority of galaxies lie within 3σ of the expected distribution (shown by the grey-shaded region), there still exists a tail of galaxies with significant offsets ($s > 3$). The number of galaxies with significant offsets is given as a fraction of total number of galaxies with that particular offset measurement. For instance, there are 14 galaxies in our sample with a measurement of [C II]-FIR continuum offset, of which two are significant, written as “[C II] vs FIR continuum (2/14)” in the top left panel.

(VUDS_COSMOS_5101218326) with no significant offset ($s < 3$) and one (DEIMOS_COSMOS_683613) with a significant offset ($s > 3$). We see that one has all centroids close together (offsets ≤ 1.2 kpc), while the other has FIR continuum centroid separated from the other centroids (offset ~ 4 kpc). As the FIR continuum traces dust, it appears that this second galaxy (DEIMOS_COSMOS_683613) has the bulk of its dust offset from stars and gas (both atomic and ionised gas as traced by [C II]). Several other significant offset galaxies are shown in Fig. A1 of Appendix A.

In Table 2, we show the number of galaxies in our sample that display such significant spatial offsets between pairs of emission tracers. We also specify the median offset and uncertainty for the full distributions of offsets, and the median of only the significant offsets in each distribution. We find the largest number of significant offsets between [C II]-UV, followed by UV-optical. This may be because the uncertainties on centroids are smaller in UV and optical, and our sample size is largest in the UV, [C II], and optical. Overall, ~ 30

percent of the galaxies in our sample (17 galaxies) show significant offsets between at least two emissions, while the remaining ~ 70 percent (37 galaxies) do not have significant offsets between any two emissions.

5 DISCUSSION

5.1 Relating spatial offsets to physical properties

We now consider the physical origin of spatial offsets in distant galaxies. Wherever possible, we plot galaxy physical properties such as specific star-formation rate (sSFR), stellar mass (M_\star), UV continuum slope (β), etc. from the Faisst et al. (2020) and Béthermin et al. (2020) catalogues against the measured spatial offsets. We then look for trends in these plots that may reveal the phenomenon that is producing spatial offsets. The galaxy physical properties were derived

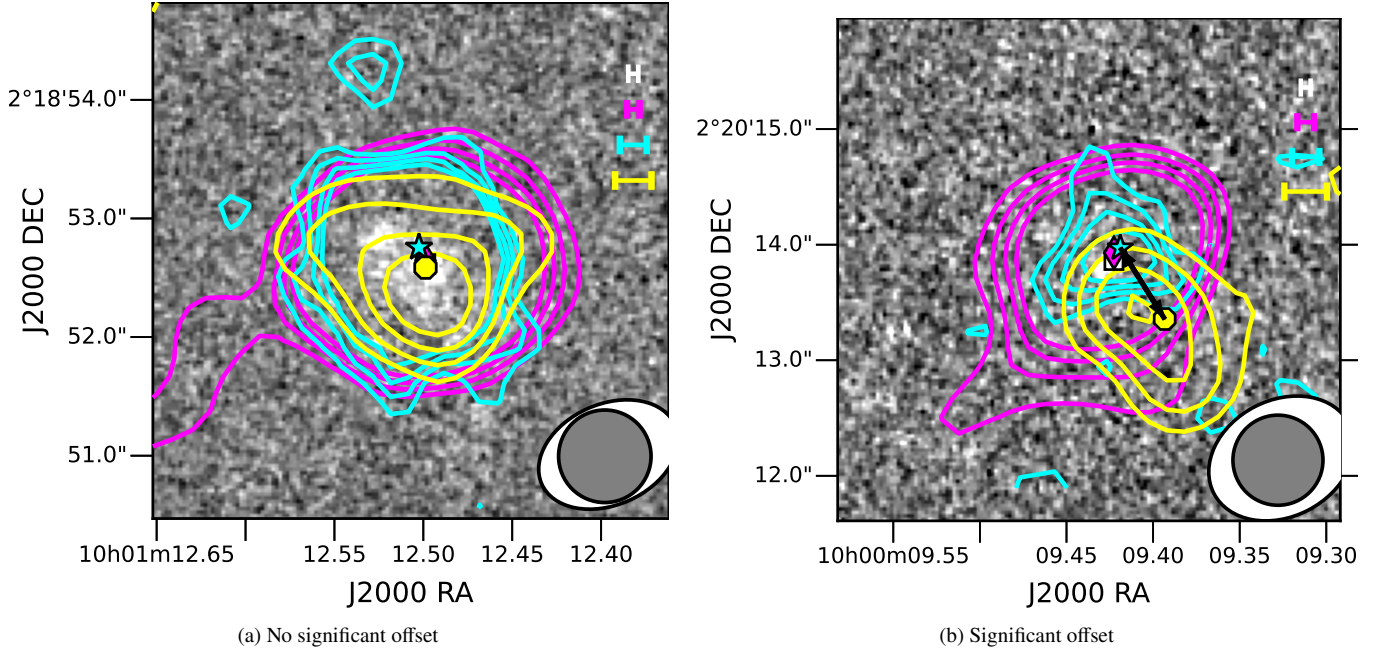


Figure 4. (a) A galaxy (VUDS_COSMOS_5101218326) with no significant offset among any of the emissions (see Sec. 4) vs (b) a galaxy (DEIMOS_COSMOS_683613) with a significant offset between FIR continuum and all other emissions. UV *HST* image is shown as a grey-scale background with [C II] (fuchsia), optical (cyan), and FIR continuum (yellow) overlaid. The contours are drawn at 2, 3, 4, and 5 times the standard deviation (calculated in an annulus with radii of 4.5 and 9.0 arcsec (30 and 60 pixels), around the centre of the image). The centroids are marked with a white square for UV emission, fuchsia diamond for [C II], cyan star for optical, and yellow octagon for FIR continuum (same colours as the respective contours), and any significant spatial offset among them is indicated by a black double-headed arrow. The calculated total error (see Sec. 3.2.5) in each emission is indicated on the top right in the same colour as the centroids. The ALMA ([C II] and FIR continuum) beam is shown as a filled white ellipse, and optical beam as a filled grey circle.

Emission tracer pair	Median offset (arcsec)	Median uncertainty (arcsec)	Number of $s > 3$ galaxies/ Total number of galaxies (percentage)	Median significant offset (arcsec)	Median significant offset (kpc)
[C II]-FIR continuum	0.13	0.17	2/14 (14 percent)	0.56	3.53
[C II]-UV	0.22	0.13	14/52 (27 percent)	0.54	3.63
FIR continuum-UV	0.24	0.16	1/16 (6 percent)	0.67	4.09
Optical-UV	0.15	0.13	3/40 (8 percent)	0.67	4.47
Optical-[C II]	0.17	0.17	2/39 (5 percent)	0.72	4.56
Optical-FIR continuum	0.3	0.19	2/13 (15 percent)	0.64	4.09

Table 2. Number of galaxies with significant spatial offsets. The first column gives the two emission tracers between which we calculate the offset. Second and third columns give the sigma-clipped medians of the full distribution of offsets and uncertainties (Sec. 3.2) respectively. Fourth column gives the number of galaxies that show significant offsets (see Sec. 4) out of the number of galaxies for which we calculate this offset, with the percentage specified in parentheses. The last column gives the sigma-clipped median of only the significant offsets both in arcsec and kpc.

via SED fitting (see Sec. 2.1) where galaxies with offsets were treated no differently than others. In the following sections, we describe several potential phenomena that may be driving the observation of spatial offsets (several of these effects may be related to each other).

5.1.1 Feedback and outflows

Feedback from star formation, supernovae, or AGN might be physically pushing the enriched gas and/or dust away from the stars (Ceverino & Klypin 2009; Maiolino et al. 2015; Katz et al. 2017; Vallini et al. 2017; Li et al. 2018; Torrey et al. 2020), which might then produce an observable spatial offset between UV/optical emission compared to the gas ([C II]) and dust emission (FIR continuum). Thus, we may expect a large offset in galaxies with high star-formation or AGN activity (assuming that enough time has elapsed since the starburst for the feedback to push the gas/dust to large galactocentric distances). As the galaxies in ALPINE are selected to have low AGN

activity (Shen et al. 2022), it is unlikely that the offsets seen here are due to AGN, but high star-formation activity can still clear out gas.

To test this idea, in Fig. 5a and 5b, we plot the stellar mass and total sSFR respectively as functions of the [C II]-UV offset. The significant offset sources in Fig. 5a display a Spearman’s rank coefficient suggesting an apparent correlation ($r_s = -0.62$), but there does not seem to be a clear distinction between galaxies with and without significant offsets. We do not observe a clear trend between offset and sSFR. Carniani et al. (2017) study the spatial offset in BDF-3299, a Lyman-break galaxy at $z=7.1$ and compare it to other observations from literature (see their fig. 6). They also do not find any clear correlations between SFR and spatial offset between [C II]/[O III] and UV.

In Fig. 5c, we now plot “burstiness” against the [C II]-UV offset. The burstiness parameter (Smit et al. 2016; Faisst et al. 2019; Atek et al. 2022) is calculated as a ratio between two SFR indicators: the H α SFR arising from young stars, and sensitive to star-formation

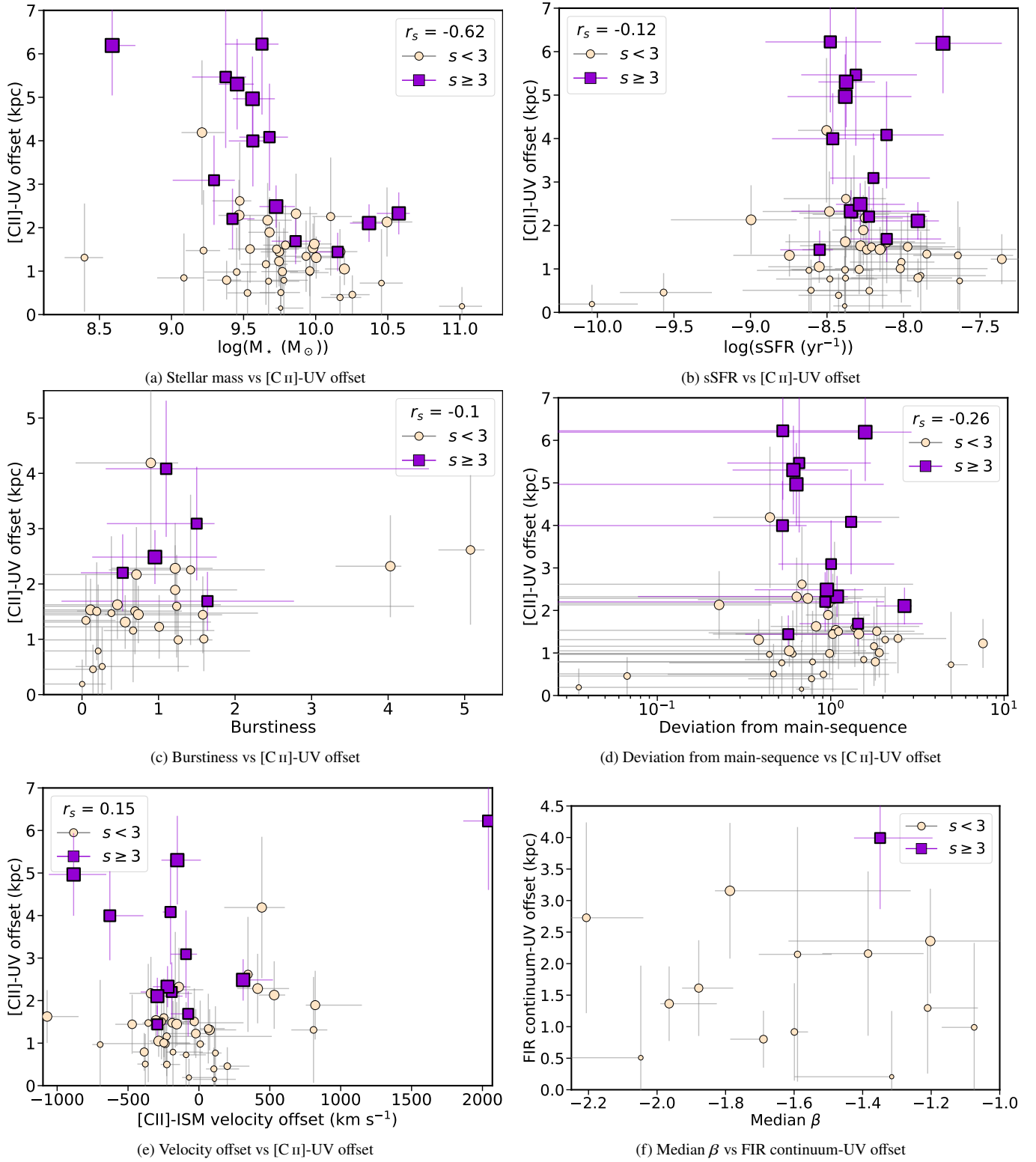


Figure 5. Relating spatial offsets with galaxy physical properties: (a) Stellar mass vs [C II]-UV (b) SED-derived sSFR vs [C II]-UV (c) burstiness vs [C II]-UV (d) deviation from main-sequence vs [C II]-UV (e) Velocity offset between ISM absorption lines and [C II] vs [C II]-UV (f) median β vs FIR continuum-UV. The measurements for the galaxies with significant offsets ($s \geq 3$; see Sec. 4) are shown as violet squares, while galaxies with no significant offsets ($s < 3$) are shown as cream-coloured circles (markersize is proportional to s). The uncertainties are plotted as violet and grey errorbars respectively. If there are three or more galaxies with significant offsets, the Spearman's rank coefficient r_s for these is also given.

on short-timescales (few Myr), and the UV SFR tracing the stellar continuum, which is sensitive to star-formation on longer timescales (few tens to hundreds of Myr). This parameter therefore measures how instantaneous the star formation is (Kennicutt & Evans 2012), with a ratio above unity suggesting a recent burst, i.e., an episode of star-formation (Atek et al. 2022). ALPINE galaxies are generally not strongly bursty, and even among those that are, we find no correlation with offset.

Next, in Fig. 5d, we plot the deviation from main-sequence against [C II]-UV offset. We compute the deviation as the ratio of the measured SFR vs that expected at the main-sequence, given the stellar mass, and assuming the Speagle et al. (2014) main-sequence relation at $z \sim 5$. We do not observe a clear correlation in this plot.

A consequence of strong feedback is gas outflow, which can be traced with [C II] emission (e.g. Ciccone et al. 2015). Large-scale outflows (e.g. Bischetti et al. 2019; Ginolfi et al. 2020; Pizzati et al. 2023; Romano et al. 2023) may be escaping the galaxy with enriched gas that glows in [C II] emission while the UV emission only traces the stars within the galaxy. Thus, the bulk of the [C II]-emitting metal-enriched gas may be located in a different region than the bulk of the UV-emitting stars. This may produce an observable offset much larger than the size (e.g. Baron et al. 2018) of the star-forming regions in the galaxy. In Fig. 5e, we plot the velocity offset between the [C II] and ISM absorption lines as a function of [C II]-UV spatial offset to check for correlation with outflow signatures. We again find no apparent trend.

5.1.2 Morphology and kinematics

As mentioned in Sec. 2.2, although we removed [C II]-identified mergers based on Romano et al. (2021), there may still be galaxies with complex optical, UV, and FIR continuum morphology, which would result in spatial offsets as described below.

5.1.2.1 Uneven star-formation Young and old stars are distributed differently in a galaxy (e.g. El Youssef et al. 2019); young stars are located only where current star-formation is taking place, while older stars (whose population grows as young stars age) are more spread out (Katz et al. 2017). UV light would trace the brightest star-forming regions (e.g. Papovich et al. 2005), whereas optical emission would include a more evenly distributed older stellar population, thereby producing an offset between the two emissions.

Some galaxies may also have non-uniform or clumpy star-formation (e.g. Guo et al. 2012; Hatsukade et al. 2015) in either UV or optical emission as can be seen for DEIMOS_COSMOS_403030 and DEIMOS_COSMOS_873756 in Appendix A Fig. A1d and A1e. In these cases, the offset illustrates a complex morphology in one of the emissions (or undetected complexity in the remaining emissions), rather than a physical separation. We require higher resolution observations at longer wavelengths than UltraVISTA K-band (with e.g. JWST) to test these scenarios by observing an even older stellar population.

5.1.2.2 Differential dust attenuation The dust distribution across the galaxy may be non-uniform (Graziani et al. 2020; Sommovigo et al. 2020), with some highly obscured and some relatively dust-free regions. In this case, the UV/optical emission from the stars within the obscured regions is almost entirely absorbed by the dust, making them invisible to *HST* and VISTA. However, ALMA can still see the re-radiated light in FIR, and hence FIR continuum remains unaffected by the obscuration. Thus, we may observe an offset between the

UV/optical emission probing only the dust-free regions compared to the FIR continuum emission probing obscured regions (e.g. Cochrane et al. 2021; Hodge et al. 2016; Behrens et al. 2018; Rivera et al. 2018). In Fig. 5f, we plot median UV continuum slope (β ; measured using Calzetti et al. (2000) spectral range; see Faisst et al. (2020)) as a function of FIR continuum-UV offset to see if offsets correlate with dust obscuration. Although, it is important to note that since the β slope is derived from UV emission, it cannot accurately measure the dust content of highly dust-obscured galaxies. Moreover, we currently only have one galaxy on this plot with a significant offset, so we require more dust continuum observations to produce large number statistics.

5.1.2.3 UV-dark or FIR-dark galaxies Considering the situation of two galaxies in a close merger (not identified as such in kinematic analyses due to the limited spatial resolution), it may be that one of them has very low dust and metallicity and hence, only emits in UV-optical (e.g. Ouchi et al. 2013; Matthee et al. 2019; Romano et al. 2022), while the other is highly dust-obscured and thus, only emits in FIR (e.g. Bowler et al. 2018; Wang et al. 2019; Romano et al. 2020; Fudamoto et al. 2021; Talia et al. 2021; Fujimoto et al. 2022b; Algera et al. 2023). Hence, *HST* will only detect the UV emitting galaxy, whereas ALMA will only detect the FIR emitting galaxy. In such a scenario, not only would we fail to identify that there are two distinct galaxies in a close merger, introducing a bias in the estimation of the real merger fraction (Romano et al. 2021), we would also derive a “spatial offset” between the UV and FIR emission from two separate galaxies. Indeed, Posses et al. (in prep.) have found evidence of such a merger in DEIMOS_COSMOS_683613 (Fig. 4b). Higher resolution observations of this galaxy from JWST and the ALMA-CRISTAL project (Herrera-Camus et al. (in prep.)) have revealed multiple components in both UV/optical and FIR emission.

Even in galaxies without such major mergers where the derived offset is consistent with the size of a typical galaxy at $z \sim 5$, i.e., a few kpc (e.g. Fujimoto et al. 2020; Ribeiro et al. 2016), there may still be distinct regions within the same galaxy. This may be the case for a few of our $s > 3$ galaxies (see Appendix B Fig. B1k), and may be the complex dust geometry scenario discussed above. In fact, sources where the offset is significantly larger than the galaxy size may be a different population than those where the offset is smaller than the galaxy size; the larger offsets may indicate environmental factors (e.g.: companion galaxies interacting) while smaller offsets may indicate processes internal to the galaxy (e.g.: disk instabilities that form clumps). Carniani et al. (2017) have proposed some other scenarios such as pristine gas inflows or past outflows with low metallicity and dust (hence invisible to ALMA), but with in-situ star formation (visible in UV), or accreting satellite clumps with obscured star-formation (visible in FIR) nearby a less obscured galaxy (visible in UV).

5.1.2.4 Kinematics Jones et al. (2021) provide a kinematic classification for a high-mass ($M_\star > 10^{9.5} M_\odot$) subset of the ALPINE sample, using various methods: the tilted ring model fitting code ^{3D}Barolo (Teodoro & Fraternali 2015), morphological classification with Gini-M20 (Lotz et al. 2004), and several disk identification criteria (Wisnioski et al. 2015). Of the 17 galaxies in our significant offset sample, seven have a classification from Jones et al. (2021), with three rotation-dominated (ROT), two dispersion-dominated (DIS), and two uncertain (UNC). The galaxies with ROT classification show significant but small offsets in our analysis (such as DEIMOS_COSMOS_396844 in Appendix A Fig. A1a). This may indicate a hidden complex morphology that is not discernible at

the current resolution. DEIMOS_COSMOS_873756 (Appendix A Fig. A1e), classified as DIS, has multiple significant offsets, between optical and all other emissions. DEIMOS_COSMOS_683613 (Fig. 4b), classified as UNC, also has multiple offsets between FIR continuum and all other emissions. However, as discussed in the previous section, this galaxy has been identified as a merging system with higher resolution (Posses et al. (in prep.)). Moreover, of the 37 galaxies in our sample with no significant offsets, three have been classified as ROT, one as DIS and eight as UNC. DEIMOS_COSMOS_881725, despite having no significant offset and ROT classification, shows multiple components in its FIR continuum image (see Fig. D.1 of Béthermin et al. 2020). It is therefore difficult to find any clear relationship between kinematic classification and significant offsets.

5.1.3 Galaxy orientation

The orientation of the galaxy on the sky may amplify the effects of uneven dust distribution (e.g. Yip et al. 2010; Devour & Bell 2017). Some galaxies may be oriented on the sky such that we can directly observe the inner star-forming regions, e.g.: a face-on spiral with dust distributed evenly across the disk. Other galaxies might be partially dust-obscured from our point of view, e.g.: an edge-on spiral with a dusty disk obscuring part of the central bulge. Whereas in the former case, centroids of the UV/optical emission and FIR continuum emission will be co-spatial, in the latter case, the UV/optical emission will arise from the unobscured part of the disk, while the FIR continuum centroid may be located near the part of the disk with the highest concentration of dust. Then, although both sources are physically the same kind of galaxy, we would interpret them as different kinds of objects based on the offset. We may be able to quantify the effects of galaxy orientation with higher spectral resolution by studying the [C II] line profile (e.g. Kohandel et al. 2019). That said, in our case, offset contribution from orientation effects is likely small given our resolution.

Overall, none of the plots in Fig. 5 show clear trends. Several more plots are presented in Appendix B, but in all cases, either the number of galaxies with significant offsets is too small to observe a correlation, or there is no definitive trend. Therefore, understanding which of these scenarios is driving the spatial offsets requires observations (e.g. Herrera-Camus et al. 2021; Chen et al. 2022; Posses et al. (in prep.)) or simulations (e.g. Graziani et al. 2020; Rizzo et al. 2022; Pallottini et al. 2022) that resolve galaxies down to sub-arcsecond scales.

5.2 Consequences of significant spatial offsets

The prevalence of significant spatial offsets in high- z galaxies may affect many commonly used relations at these redshifts. For instance, significant offsets between [C II] and UV emission could alter the [C II]-SFR relation (Schaerer et al. 2020; Romano et al. 2022; Ferrara et al. 2022) as the [C II] emission would arise from gas that is tracing a different region, away from the site of star formation. In Fig. 6, we plot the $L_{\text{[C II]}}$ -SFR relation and highlight the galaxies with significant [C II]-UV offsets. We see that the galaxies with significant offsets tend to lie above those without, thereby affecting the overall relation. This may indicate that the SED-derived SFR is underestimated for galaxies with offsets, possibly due to missing or undetected emission.

Similarly, FIR-UV offsets would affect the IRX- β relation (e.g. Faisst et al. 2017; Popping et al. 2017; Narayanan et al. 2018; Fudamoto et al. 2020; Sommovigo et al. 2020; Boquien et al. 2022).

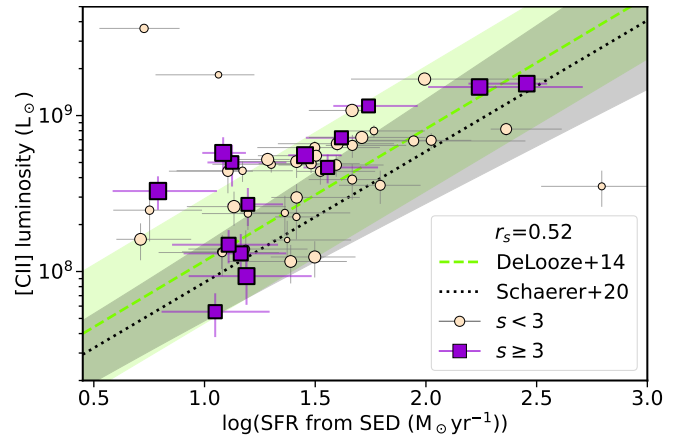


Figure 6. The $L_{\text{[C II]}}$ -SFR relation for galaxies with and without significant spatial offsets. As in Fig. 5, the galaxies with a significant [C II]-UV offset are shown as violet squares with errorbars in the same colour, while those without significant offsets are shown as cream-coloured circles with errorbars in grey. Markersize increases with significance. The relations from De Looze et al. (2014) and Schaerer et al. (2020) are plotted as green dashed and black dotted lines respectively. The corresponding uncertainty in these relations is shown as shaded regions in the same colour.

UV emission is used to get IRX- β , which is then assumed to be the dust content in FIR, but if emission does not originate in the same physical region in the galaxy (e.g. Casey et al. 2014; Gómez-Guijarro et al. 2018; Elbaz et al. 2018), this assumption does not hold.

Many galaxy SED modelling codes (e.g. CIGALE (Burgarella et al. 2005; Noll et al. 2009; Boquien et al. 2019; Pacifici et al. 2023), MAGPHYS (Da Cunha et al. 2008)) assume an energy balance between UV and FIR emission, which may not hold in the presence of offsets, thereby affecting SED-derived estimates of stellar mass and SFR. Ferrara et al. (2022) define a dimensionless quantity called the molecular index, which is a ratio between the IR-to-UV continuum flux and the difference between observed and intrinsic β slopes. This quantity measures the extent to which IR and UV emission are decoupled. Sommovigo et al. (2022) study the ALPINE sample and find that SED derived SFRs do not match the total (including UV and IR) SFRs for galaxies that have a high molecular index, which they interpret as a consequence of spatially decoupled UV and IR emission. The galaxy with the largest discrepancy in their analysis (DEIMOS_COSMOS_873756; shown in Appendix A Fig. A1e) is one of the galaxies we find to have a significant spatial offset. Using higher resolution observations, Mitsuhashi et al. (2023) similarly find a significant difference between SED-derived SFR and total SFR of this galaxy (called CRISTAL-24 in their sample). Our results lend support to the idea put forth by these works of spatially decoupled IR and UV emission in this galaxy.

On the other hand, Haskell et al. (2023) tested the effect of offsets with MAGPHYS, and found that offsets, however large, have no appreciable impact on SED-derived properties (provided an acceptable fit is obtained) in over 80 percent of their sample. They propose that the underlying Charlot & Fall (2000) dust model has sufficient flexibility to account for the differential dust attenuation between the decoupled UV-bright and FIR-bright regions of the galaxies with offsets.

In any case, deviations (if any) caused by spatial offsets can be mitigated via spatially resolved SED modelling (e.g. Wuyts et al. 2012; Sorba & Sawicki 2018).

The presence of offsets may also affect follow-up ALMA obser-

vations of JWST targets (or vice-versa). If there is a spatial offset, this should be considered when planning observations and interpreting data. For instance, JWST/NIRSpec has a slit width of only ~ 0.2 arcsec (Jakobsen et al. 2022), comparable to our median uncertainties, and much smaller than our median significant offsets (see Table 2). Large surveys with this instrument, e.g. Cosmic Evolution Early Release Science (CEERS Finkelstein et al. 2023), JWST Advanced Deep Extragalactic Survey (JADES Eisenstein et al. 2023), might only observe the UV emission, and miss the dusty component. Therefore, spatial offsets must be taken into account for all studies, not just spatially resolved galaxy modelling.

6 SUMMARY AND CONCLUSIONS

We study a sample of main-sequence star-forming galaxies at $z \sim 4-6$ from the ALPINE dataset. We identify 54 galaxies that were detected in [C II] and FIR continuum emission in ALMA data, UV emission in *HST* data, and optical emission in K-band UltraVISTA data, excluding [C II]-mergers or multi-component systems based on Romano et al. (2021) and Jones et al. (2021).

We use the *HST* coordinates (with astrometric correction) from Faisst et al. (2020) as the UV centroids. To calculate [C II], FIR continuum, and optical centroids, we fit 2D Gaussians to the detected emission and apply a bootstrapping technique to estimate fit centroids and uncertainties. We convolve the positional accuracy of the respective telescopes and ALMA noise correlation uncertainty with the fit uncertainty to calculate the total uncertainty. We then estimate the spatial offset between centroids of detected emission for each galaxy, along with offset significance (s), which is calculated as the measured offset divided by the total uncertainty on the offset.

- The (sigma-clipped) median of the measured offsets is 0.1–0.3 arcsec, which translates to $\sim 0.6-2$ kpc at our median redshift of $z \sim 5$.
- We establish a cut-off of $s > 3$ to define “significant” offsets. These significant offsets are $\sim 0.5-0.7$ arcsec, or $\sim 3.5-4.5$ kpc.
- 17 galaxies (~ 30 percent of the sample) display significant offsets between one or more emission pairs, although none have all four emissions offset from each other. The remaining 37 galaxies (~ 70 percent of the sample) have no significant offsets.
- We discuss several potential phenomena that may lead to the observation of spatial offsets, plotting corresponding galaxy physical properties against their measured spatial offsets wherever possible. We find no clear trends or the statistics are too low to make strong conclusions. The physical origin of the observed offsets is therefore still unclear.

The existence of significant spatial offsets in ~ 30 percent of our sample indicates that it is possible for main-sequence galaxies at $z \sim 4-6$ to have the bulk of the stars spatially offset from the bulk of the interstellar medium. Future simulations and observations must therefore take into account that the emission observed across wavelengths may be coming from different, spatially segregated regions of the galaxy.

We require large number statistics and higher resolution observations and simulations to identify the processes driving spatial offsets. For instance, we could perform this analysis on the REBELS sample (already shown to have spatial offsets in Inami et al. 2022), which has different SFRs and M_\star , but similar angular resolution as ALPINE. *JWST*, with its superior angular resolution, may also be able to shed light on the origin of offsets (e.g. Bakx et al. 2023).

ACKNOWLEDGEMENTS

We thank the anonymous referee for insightful comments, and Kate Whitaker, Francesca Rizzo, and Ana Posses for useful discussions. The Cosmic Dawn Center is funded by the Danish National Research Foundation under grant number 140. M.K. was supported by the ANID BASAL project FB210003. This publication has received funding from the European Union’s Horizon 2020 research and innovation programme under grant agreement No 101004719 (ORP). M.R. acknowledges support from the Narodowe Centrum Nauki (UMO-2020/38/E/ST9/00077) and support from the Foundation for Polish Science (FNP) under the program START 063.2023. E.I. acknowledges funding by ANID FONDECYT Regular 1221846. GCJ acknowledges funding from the “FirstGalaxies” Advanced Grant from the European Research Council (ERC) under the European Union’s Horizon 2020 research and innovation programme (Grant agreement No. 789056). M.B. acknowledges support from FONDECYT regular grant 1211000 and by the ANID BASAL project FB210003. 021-001131-S funded by MCIN/AEI/10.13039/501100011033. H.M.H. acknowledges support from National Fund for Scientific and Technological Research of Chile (FONDECYT) through grant no. 3230176

This paper is based on data obtained with the ALMA Observatory, under Large Program 2017.1.00428.L. ALMA is a partnership of ESO (representing its member states), NSF (USA) and NINS (Japan), together with NRC (Canada), MOST and ASIAA (Taiwan), and KASI (Republic of Korea), in cooperation with the Republic of Chile. The Joint ALMA Observatory is operated by ESO, AUI/NRAO and NAOJ. This paper makes use of archival data from the NASA/ESA *Hubble Space Telescope*. Based on data obtained with the European Southern Observatory Very Large Telescope, Paranal, Chile, under Large Program 185.A-0791, and made available by the VUDS team at the CESAM data centre, Laboratoire d’Astrophysique de Marseille, France. This work is based on observations taken by the 3D-HST Treasury Program (GO12177 and 12328) with the NASA/ESA *HST*, which is operated by the Association of Universities for Research in Astronomy, Inc., under NASA contract NAS5-26555. Based on data products from observations made with ESO Telescopes at the La Silla Paranal Observatory under ESO programme ID 179.A-2005 and on data products produced by TERAPIX and the Cambridge Astronomy Survey Unit on behalf of the UltraVISTA consortium.

DATA AVAILABILITY

The data used in the paper are available in the ALMA archive at <https://almascience.nrao.edu> under the program ID 2017.1.00428.L. The derived data and models generated in this research will be shared on reasonable request to the corresponding author.

REFERENCES

- Algera H. S. B., et al., 2023, *Monthly Notices of the Royal Astronomical Society*, 527, 6867
- Arata S., Yajima H., Nagamine K., Li Y., Khochfar S., 2019, *Monthly Notices of the Royal Astronomical Society*, 488, 2629
- Arnouts S., Ilbert O., 2011, *Astrophysics Source Code Library*, record ascl:1108.009, p. ascl:1108.009
- Arnouts S., Cristiani S., Moscardini L., Matarrese S., Lucchin F., Fontana A., Giallongo E., 1999, *Monthly Notices of the Royal Astronomical Society*, 310, 540
- Atek H., Furtak L., Oesch P., van Dokkum P., Reddy N., Contini T., Illingworth

- G., Wilkins S., 2022, *Monthly Notices of the Royal Astronomical Society*, 511, 4464
- Bakx T. J. L. C., et al., 2023, *Monthly Notices of the Royal Astronomical Society*, 519, 5076
- Baron D., et al., 2018, *Monthly Notices of the Royal Astronomical Society*, 480, 3993
- Behrens C., Pallottini A., Ferrara A., Gallerani S., Vallini L., 2018, *Monthly Notices of the Royal Astronomical Society*, 477, 552
- Béthermin M., et al., 2020, *Astronomy & Astrophysics*, 643, A2
- Bischetti M., Maiolino R., Carniani S., Fiore F., Piconcelli E., Fluetsch A., 2019, *Astronomy & Astrophysics*, 630, A59
- Boquien M., Burgarella D., Roehlly Y., Buat V., Ciesla L., Corre D., Inoue A. K., Salas H., 2019, *Astronomy and Astrophysics*, 622, A103
- Boquien M., et al., 2022, *Astronomy and Astrophysics*, 663
- Bowler R. A., Bourne N., Dunlop J. S., McLure R. J., McLeod D. J., 2018, *Monthly Notices of the Royal Astronomical Society*, 481, 1631
- Bowler R. A. A., Cullen F., McLure R. J., Dunlop J. S., Avison A., 2022, *Monthly Notices of the Royal Astronomical Society*, 510, 5088
- Bruzual G., Charlot S., 2003, *Monthly Notices of the Royal Astronomical Society*, 344, 1000
- Burgarella D., Buat V., Iglesias-Páramo J., 2005, *Monthly Notices of the Royal Astronomical Society*, 360, 1413
- Calzetti D., Armus L., Bohlin R. C., Kinney A. L., Koornneef J., Storchi-Bergmann T., 2000, *The Astrophysical Journal*, 533, 682
- Cardamone C. N., et al., 2010, *The Astrophysical Journal Supplement Series*, 189, 270
- Carilli C., Walter F., 2013, *Annual Review of Astronomy and Astrophysics*, 51, 105
- Carniani S., et al., 2017, *Astronomy and Astrophysics*, 605, A42
- Carniani S., et al., 2018, *Monthly Notices of the Royal Astronomical Society*, 478, 1170
- Casey C. M., et al., 2014, *Astrophysical Journal*, 796, 95
- Cassata P., et al., 2020, *Astronomy & Astrophysics*, 643, A6
- Ceverino D., Klypin A., 2009, *The Astrophysical Journal*, 695, 292
- Charlot S., Fall S. M., 2000, *The Astrophysical Journal*, 539, 718
- Chen Z., Stark D. P., Endsley R., Topping M., Whitler L., Charlot S., 2022, *Monthly Notices of the Royal Astronomical Society*, 518, 5607
- Cicone C., et al., 2015, *Astronomy & Astrophysics*, 574, A14
- Cochrane R. K., et al., 2021, *Monthly Notices of the Royal Astronomical Society*, 503, 2622
- Da Cunha E., Charlot S., Elbaz D., 2008, *Monthly Notices of the Royal Astronomical Society*, 388, 1595
- Dayal P., Ferrara A., Dayal P., Ferrara A., 2018, *PhR*, 780, 1
- De Looze I., et al., 2014, *Astronomy and Astrophysics*, 568, A62
- Devour B. M., Bell E. F., 2017, *Monthly Notices of the Royal Astronomical Society: Letters*, 468, L31
- Eisenstein D. J., et al., 2023, *arxiv*: 2306.02465
- El Youssoufi D., et al., 2019, *Monthly Notices of the Royal Astronomical Society*, 490, 1076
- Elbaz D., et al., 2018, *Astronomy and Astrophysics*, 616, A110
- Faisst A. L., et al., 2017, *The Astrophysical Journal*, 847, 21
- Faisst A. L., Capak P. L., Emami N., Tacchella S., Larson K. L., 2019, *The Astrophysical Journal*, 884, 133
- Faisst A. L., et al., 2020, *The Astrophysical Journal Supplement Series*, 247, 61
- Fan X., Carilli C., Keating B., 2006, *Annual Review of Astronomy and Astrophysics*, 44, 415
- Ferrara A., et al., 2022, *Monthly Notices of the Royal Astronomical Society*, 512, 58
- Finkelstein S. L., et al., 2023, *The Astrophysical Journal Letters*, 946, L13
- Förster Schreiber N. M., Wuyts S., 2020, *Annual Review of Astronomy and Astrophysics*, 58, 661
- Fudamoto Y., et al., 2020, *Astronomy and Astrophysics*, 643
- Fudamoto Y., et al., 2021, *Nature*, 597, 489
- Fujimoto S., et al., 2020, *The Astrophysical Journal*, 900, 1
- Fujimoto S., et al., 2022a, *arXiv*, p. arXiv:2212.06863
- Fujimoto S., et al., 2022b, *Nature*, 604, 261
- Giavalisco M., Team t. G., 2003, *The Astrophysical Journal*, 600, L93
- Giolfi M., et al., 2020, *Astronomy & Astrophysics*, 633, A90
- Gómez-Guijarro C., et al., 2018, *The Astrophysical Journal*, 856, 121
- Graziani L., Schneider R., Giolfi M., Hunt L. K., Maio U., Glatzle M., Ciardi B., 2020, *Monthly Notices of the Royal Astronomical Society*, 494, 1071
- Gruppioni C., et al., 2020, *Astronomy and Astrophysics*, 643, A8
- Guo Y., Giavalisco M., Ferguson H. C., Cassata P., Koekemoer A. M., 2012, *Astrophysical Journal*, 757, 120
- Haskell P., Smith D. J. B., Cochrane R. K., Hayward C. C., Anglés-Alcázar D., 2023, *Monthly Notices of the Royal Astronomical Society*, 525, 1535
- Hatsukade B., Tamura Y., Iono D., Matsuda Y., Hayashi M., Oguri M., 2015, *Publications of the Astronomical Society of Japan*, 67
- Herrera-Camus R., et al., 2021, *Astronomy and Astrophysics*, 649
- Hodge J. A., Carilli C. L., Walter F., De Blok W. J., Riechers D., Daddi E., Lentati L., 2012, *Astrophysical Journal*, 760, 11
- Hodge J. A., et al., 2016, *The Astrophysical Journal*, 833, 103
- Hollenbach D. J., Tielens A. G. G. M., 1999, *RvMP*, 71, 173
- Ilbert O., et al., 2006, *Astronomy and Astrophysics*, 457, 841
- Inami H., et al., 2022, *Monthly Notices of the Royal Astronomical Society*, 515, 3126
- Jakobsen P., et al., 2022, *Astronomy & Astrophysics*, 661, A80
- Jones G. C., et al., 2021, *Monthly Notices of the Royal Astronomical Society*, 507, 3540
- Katz H., Kimm T., Sijacki D., Haehnelt M. G., 2017, *Monthly Notices of the Royal Astronomical Society*, 468, 4831
- Katz H., et al., 2019, *Monthly Notices of the Royal Astronomical Society*, 487, 5902
- Kennicutt R. C., 1998, *Annual Review of Astronomy and Astrophysics*, 36, 189
- Kennicutt R. C., Evans N. J., 2012, *Annual Review of Astronomy and Astrophysics*, 50, 531
- Koekemoer A. M., et al., 2007, *The Astrophysical Journal Supplement Series*, 172, 196
- Koekemoer A. M., et al., 2011, *The Astrophysical Journal Supplement Series*, 197, 36
- Kohandel M., Pallottini A., Ferrara A., Zanella A., Behrens C., Carniani S., Gallerani S., Vallini L., 2019, *Monthly Notices of the Royal Astronomical Society*, 487, 3007
- Lagache G., Cousin M., Chatzikos M., 2018, *Astronomy & Astrophysics*, 609, A130
- Laporte N., et al., 2017, *The Astrophysical Journal*, 837, L21
- Le Fèvre O., et al., 2020, *Astronomy & Astrophysics*, 643, A1
- Li Y.-P., et al., 2018, *The Astrophysical Journal*, 866, 70
- Lotz J. M., Primack J., Madau P., 2004, *The Astronomical Journal*, 128, 163
- Maiolino R., et al., 2015, *Monthly Notices of the Royal Astronomical Society*, 452, 54
- Matthee J., et al., 2019, *The Astrophysical Journal*, 881, 124
- McCracken H. J., et al., 2012, *Astronomy and Astrophysics*, 544
- McMullin J. P., Waters B., Schiebel D., Young W., Golap K., 2007, *Astronomical Data Analysis Software and Systems XVI*, 376, 127
- Mignard F., et al., 2018, *Astronomy & Astrophysics*, 616, A14
- Mitsuhashi I., et al., 2023, *arXiv*, 17, arXiv:2311.17671
- Moneti A., et al., 2019, *ESO Science Archive Facility - Phase 3 Data Release Description*
- Moneti A., et al., 2023, *VizieR Online Data Catalog*, p. II/373
- Narayanan D., Davé R., Johnson B. D., Thompson R., Conroy C., Geach J., 2018, *Monthly Notices of the Royal Astronomical Society*, 474, 1718
- Noeske K. G., et al., 2007, *The Astrophysical Journal*, 660, L43
- Noll S., Burgarella D., Giovannoli E., Buat V., Marcellac D., Muñoz-Mateos J. C., 2009, *Astronomy & Astrophysics*, 507, 1793
- Ouchi M., et al., 2013, *The Astrophysical Journal*, 778, 102
- Pacifici C., et al., 2023, *The Astrophysical Journal*, 944, 141
- Pallottini A., et al., 2019, *Monthly Notices of the Royal Astronomical Society*, 487, 1689
- Pallottini A., et al., 2022, *Monthly Notices of the Royal Astronomical Society*, 513, 5621
- Papovich C., Dickinson M., Giavalisco M., Conselice C. J., Ferguson H. C., 2005, *The Astrophysical Journal*, 631, 101
- Pentericci L., et al., 2016, *The Astrophysical Journal*, 829, L11

- Pizzati E., Ferrara A., Pallottini A., Sommovigo L., Kohandel M., Carniani S., 2023, *Monthly Notices of the Royal Astronomical Society*, 519, 4608
- Popesso P., et al., 2022, *Monthly Notices of the Royal Astronomical Society*, 519, 1526
- Popping G., Puglisi A., Norman C. A., 2017, *Monthly Notices of the Royal Astronomical Society*, 472, 2315
- Pozzi F., et al., 2021, *Astronomy & Astrophysics*, 653, A84
- Ribeiro B., et al., 2016, *Astronomy & Astrophysics*, 593, A22
- Rivera G. C., et al., 2018, *The Astrophysical Journal*, 863, 56
- Rizzo F., Kohandel M., Pallottini A., Zanella A., Ferrara A., Vallini L., Toft S., 2022, *Astronomy & Astrophysics*, 667, A5
- Robertson B. E., 2022, *Annual Review of Astronomy and Astrophysics*, 60, 121
- Romano M., et al., 2020, *Monthly Notices of the Royal Astronomical Society*, 496, 875
- Romano M., et al., 2021, *Astronomy and Astrophysics*, 653, A111
- Romano M., et al., 2022, *Astronomy & Astrophysics*, 660, A14
- Romano M., et al., 2023, *Astronomy & Astrophysics*, 677, A44
- Schaerer D., et al., 2020, *Astronomy & Astrophysics*, 643, A3
- Schouws S., et al., 2022, *The Astrophysical Journal*, 928, 31
- Scoville N., et al., 2006a, *The Astrophysical Journal Supplement Series*, 172, 1
- Scoville N., et al., 2006b, *The Astrophysical Journal Supplement Series*, 172, 38
- Shen L., et al., 2022, *The Astrophysical Journal*, 935, 177
- Smit R., Bouwens R. J., Labbé I., Franx M., Wilkins S. M., Oesch P. A., 2016, *The Astrophysical Journal*, 833, 254
- Sommovigo L., Ferrara A., Pallottini A., Carniani S., Gallerani S., Decataldo D., 2020, *Monthly Notices of the Royal Astronomical Society*, 497, 956
- Sommovigo L., et al., 2022, *Monthly Notices of the Royal Astronomical Society*, 517, 5930
- Sorba R., Sawicki M., 2018, *Monthly Notices of the Royal Astronomical Society*, 476, 1532
- Speagle J. S., Steinhardt C. L., Capak P. L., Silverman J. D., 2014, *Astrophysical Journal, Supplement Series*, 214
- Talia M., Cimatti A., Giulietti M., Zamorani G., Bethermin M., Faisst A., Fèvre O. L., Smolčić V., 2021, *The Astrophysical Journal*, 909, 23
- Teodoro E. M. D., Fraternali F., 2015, *Monthly Notices of the Royal Astronomical Society*, 451, 3021
- The Astropy Collaboration et al., 2022, *The Astrophysical Journal*, 935, 167
- Torrey P., et al., 2020, *Monthly Notices of the Royal Astronomical Society*, 497, 5292
- Vallini L., Gallerani S., Ferrara A., Baek S., 2013, *Monthly Notices of the Royal Astronomical Society*, 433, 1567
- Vallini L., Ferrara A., Pallottini A., Gallerani S., 2017, *Monthly Notices of the Royal Astronomical Society*, 467, 1300
- Virtanen P., et al., 2020, *Nature Methods* 2020 17:3, 17, 261
- Wang T., et al., 2019, *Nature*, 572, 211
- Willott C. J., Carilli C. L., Wagg J., Wang R., 2015, *Astrophysical Journal*, 807
- Wisnioski E., et al., 2015, *The Astrophysical Journal*, 799, 209
- Wolfire M. G., Vallini L., Chevance M., 2022, *Annual Review of Astronomy and Astrophysics*, 60, 247
- Wuyts S., et al., 2012, *Astrophysical Journal*, 753, 114
- Yip C.-W., Szalay A. S., Wyse R. F. G., Dobos L., Budavári T., Csabai I., 2010, *The Astrophysical Journal*, 709, 780
- Zanella A., et al., 2018, *Monthly Notices of the Royal Astronomical Society*, 481, 1976

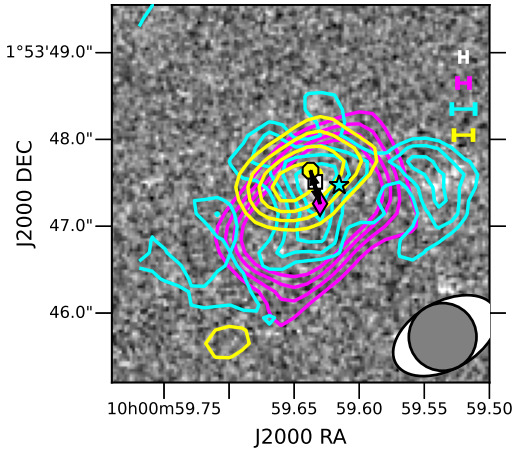
APPENDIX A: GALAXIES WITH SIGNIFICANT OFFSETS

In Fig. A1, we show several galaxies from our sample for which we measure significant offsets. UV images are shown in grey-scale, and [C II], optical, and FIR continuum (where available) are over-plotted as coloured contours. The colour scheme is the same as Fig. 4 in the main text.

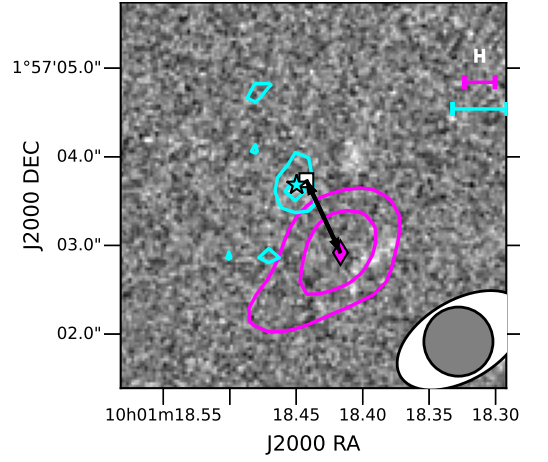
APPENDIX B: OFFSETS VS SELECTED PHYSICAL PROPERTIES

In Figs. B1–B1, we plot our measured spatial offsets among [C II], UV, optical, and FIR continuum emission against a range of galaxy physical properties. Colour scheme is the same as in Fig. 5 in the main text. Galaxies with significant offsets do not display any clear trends with any of the physical properties, compared to those without significant offsets.

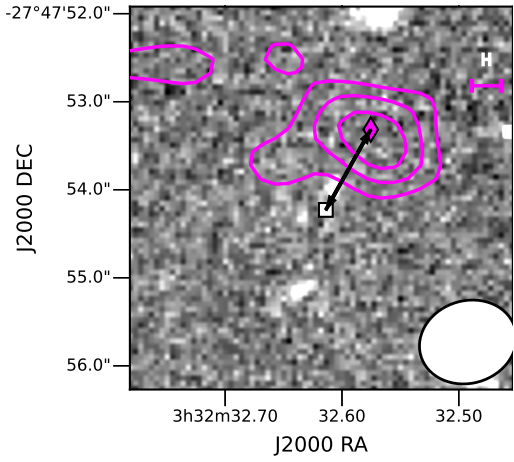
This paper has been typeset from a \LaTeX file prepared by the author.



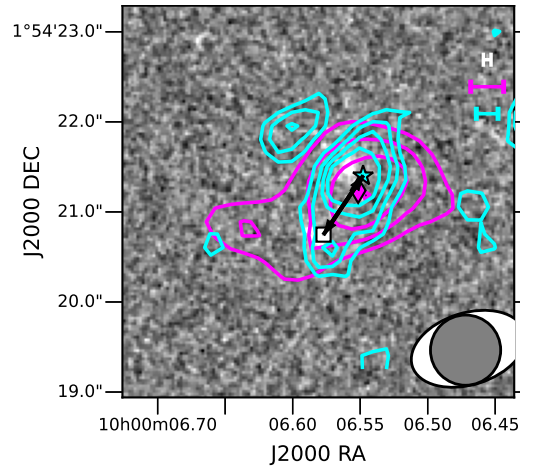
(a) Significant [C II]-FIR continuum offset in DEIMOS_COSMOS_396844



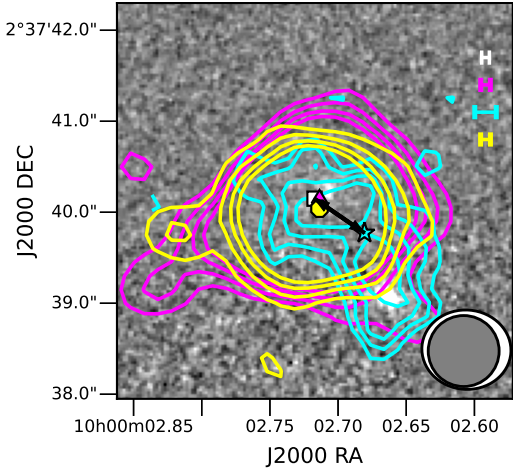
(b) Significant [C II]-UV offset in DEIMOS_COSMOS_430951



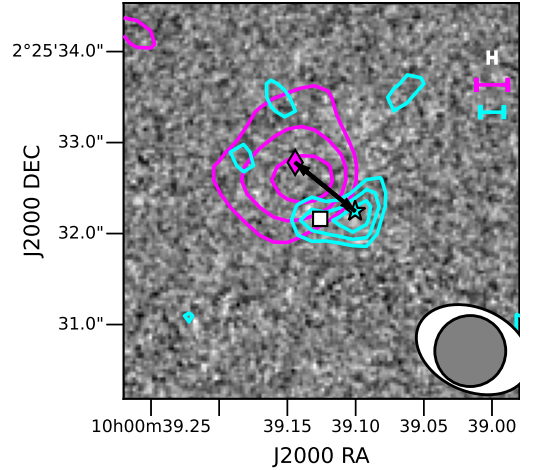
(c) Significant [C II]-UV offset in CANDELS_GOODSS_75



(d) Significant Optical-UV offset in DEIMOS_COSMOS_403030



(e) Significant Optical-UV offset in DEIMOS_COSMOS_873756



(f) Significant Optical-[C II] offset in DEIMOS_COSMOS_742174

Figure A1. Galaxies with significant offsets. Colour scheme is the same as Fig. 4. UV *HST* image is shown as a grey-scale background with [C II] (fuchsia), optical (cyan), and FIR continuum (yellow) overlaid. The contours are drawn at 2, 3, 4, and 5 times the standard deviation. The centroids are marked with a white square for UV emission, fuchsia diamond for [C II], cyan star for optical, and yellow octagon for FIR continuum (same colours as the respective contours), and the spatial offset among them is indicated by a black double-headed arrow. The calculated total error in each emission is indicated on the top right in the same colour as the contours. The ALMA ([C II] and FIR continuum) beam is shown as a filled white ellipse, and optical beam as a filled grey circle.

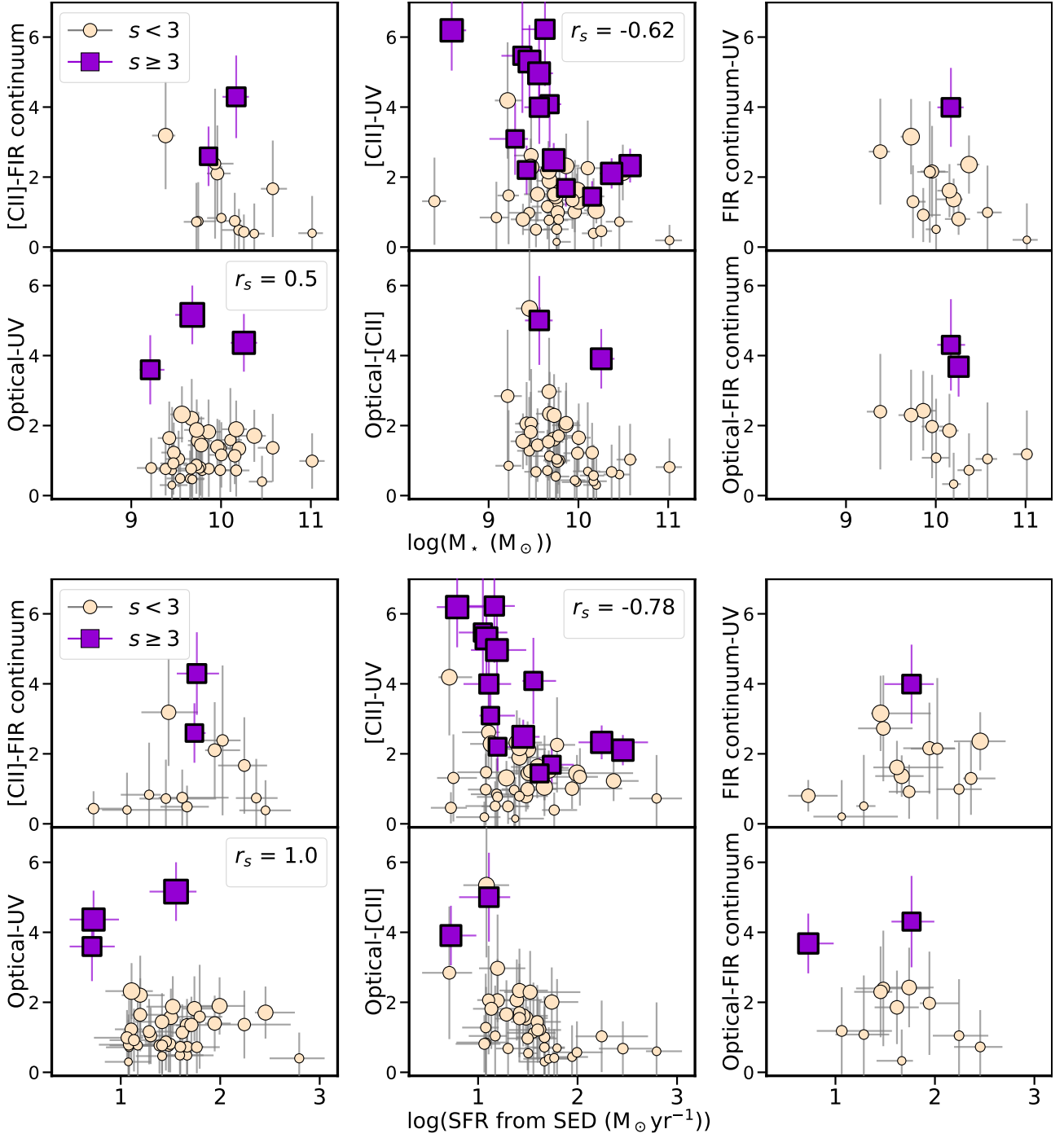


Figure B1. Offsets (in kpc) vs physical properties a) $\log(\text{Stellar mass})$ b) Total SFR. Colour scheme is the same as in Fig. 5. Galaxies with significant offsets are shown as purple squares, while those without significant offsets are shown as cream-coloured circles. Marker-size increases with significance. The Spearman's rank coefficient (r_s) is given whenever there are three or more galaxies with significant offsets.

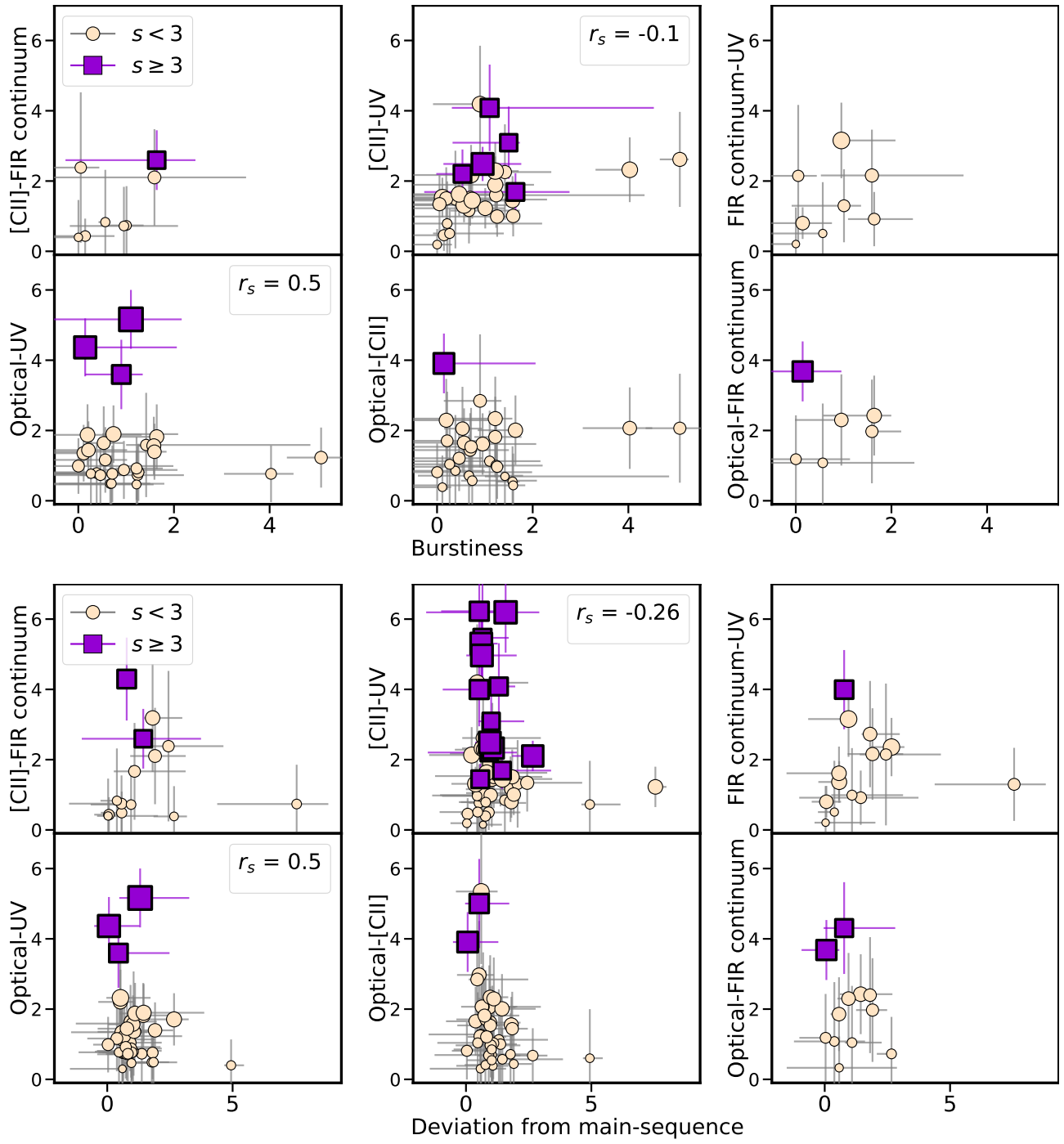


Figure B1. (contd.) c) Burstiness (as in Fig. 5c) d) deviation from main-sequence (as in Fig. 5d)

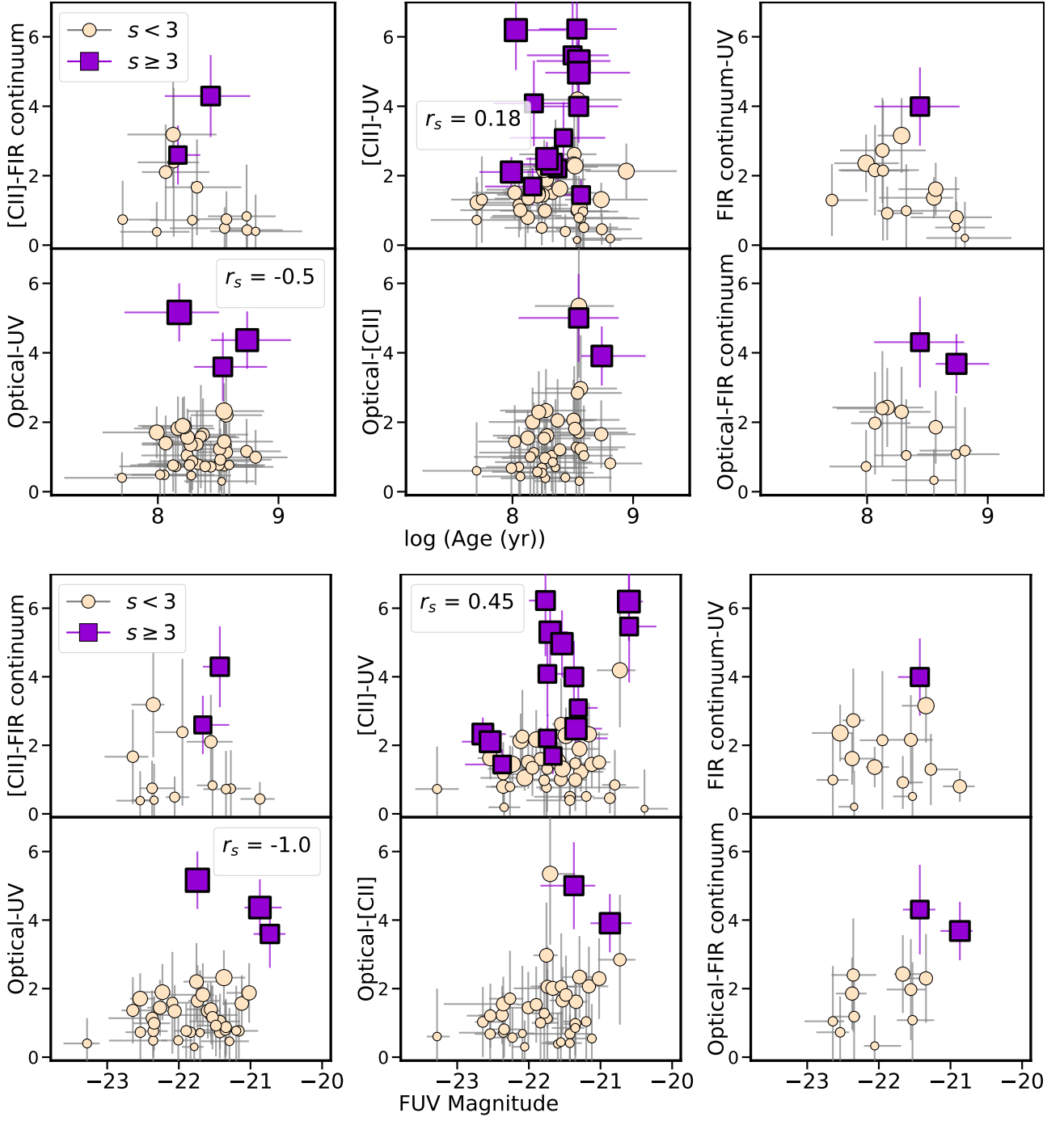


Figure B1. (contd.) e) log(Age) f) FUV magnitude

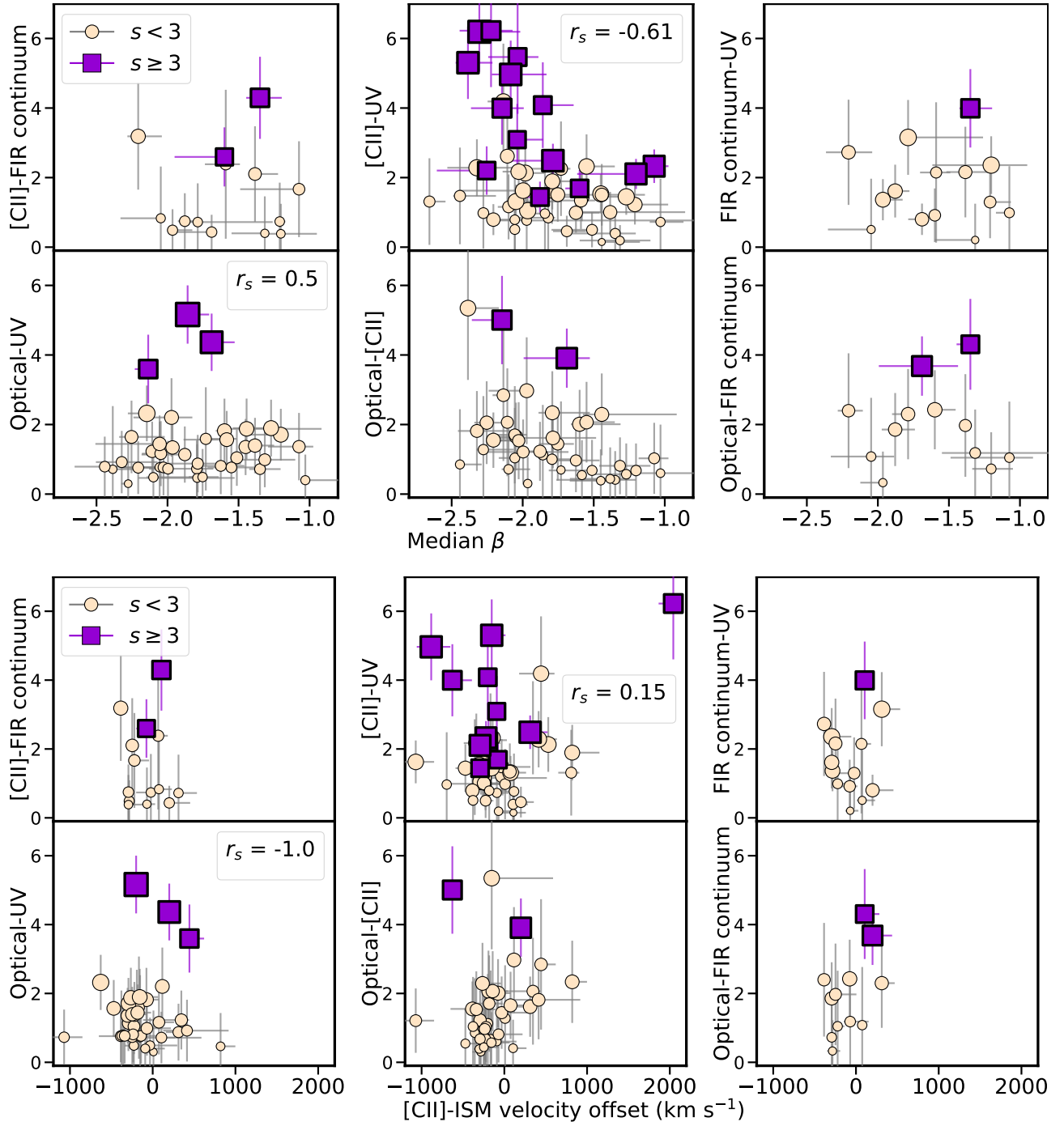


Figure B1. (contd.) g) median UV continuum slope β (as in Fig. 5f) h) Ly α -[C II] velocity offset (as in Fig. 5e)

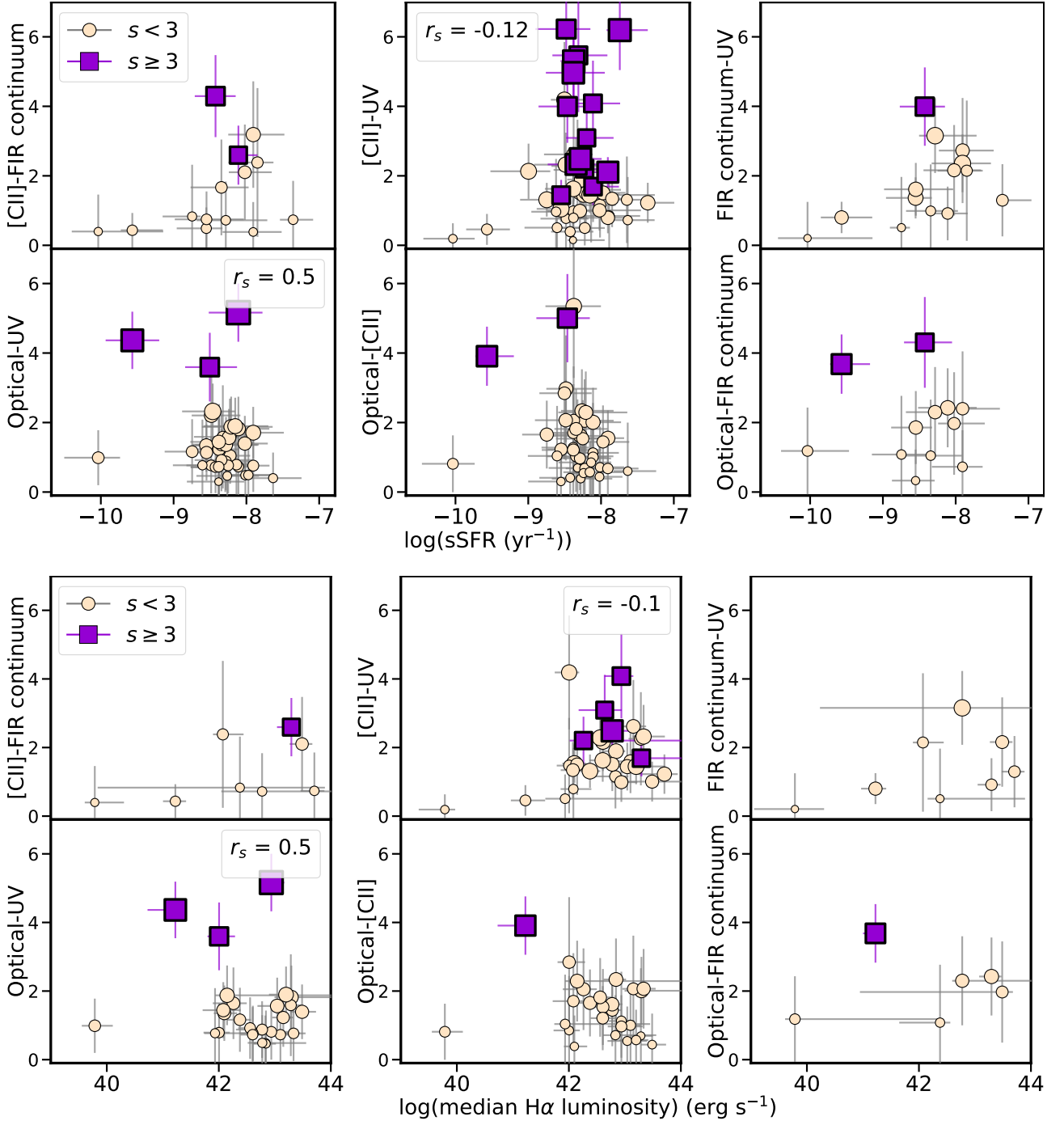


Figure B1. (contd.) i) Total specific SFR, j) median H α luminosity

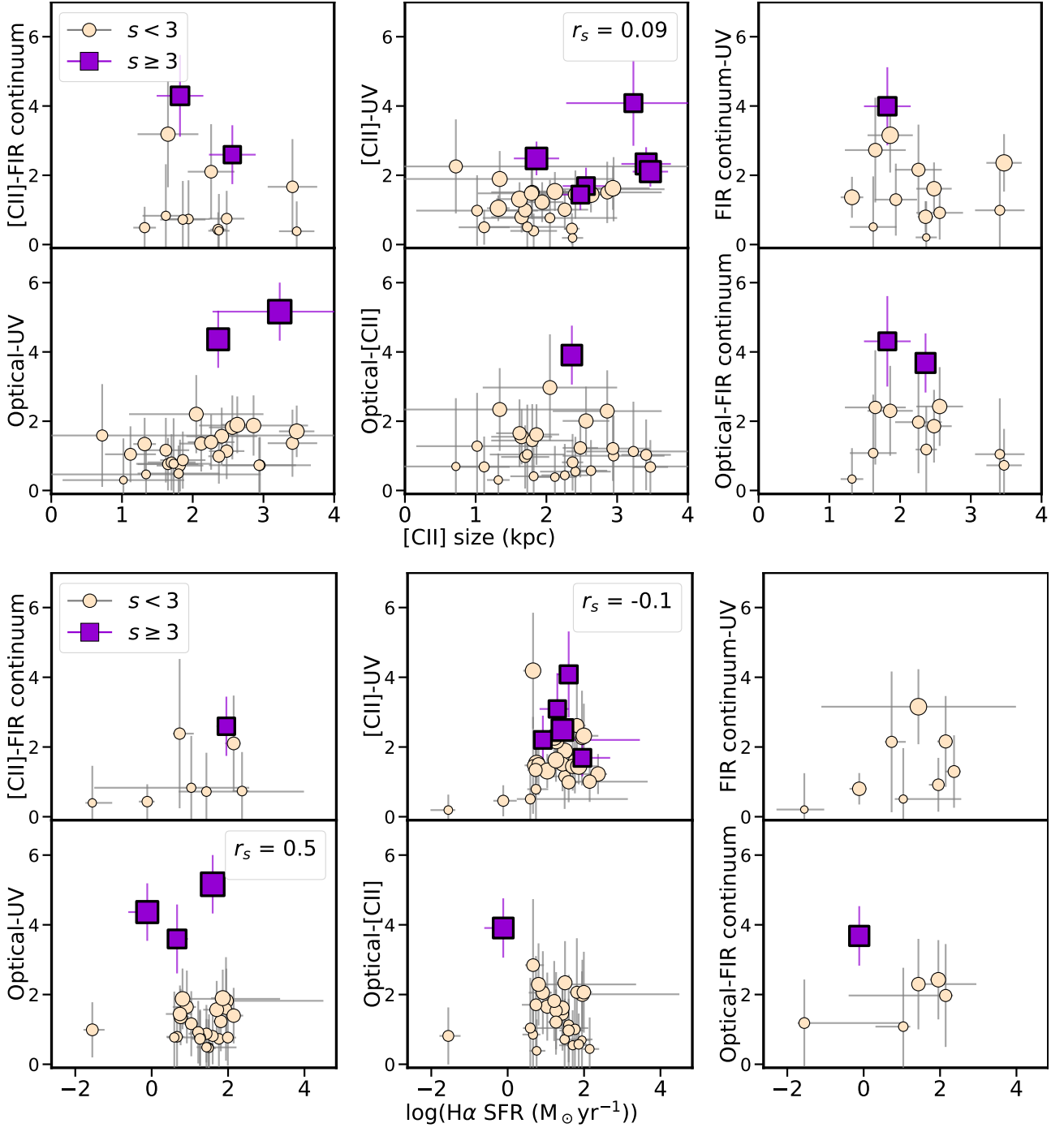


Figure B1. (contd.) k) [C II] size in kpc l) $\text{H}\alpha$ SFR in $M_{\odot} \text{ yr}^{-1}$